Quasinormal-mode filters: A new approach to analyze the gravitational-wave ringdown of binary black-hole mergers

Sizheng Ma,[1,*] Keefe Mitman,[1] Ling Sun,[2] Nils Deppe,[1] François Hébert,[1] Lawrence E. Kidder,[3] Jordan Moxon,[1] William Throwe,[3] Nils L. Vu,[4] and Yanbei Chen[1]

[1]*TAPIR 350-17, California Institute of Technology, 1200 E California Boulevard, Pasadena, California 91125, USA*
[2]*OzGrav-ANU, Centre for Gravitational Astrophysics, College of Science, The Australian National University, Australian Capital Territory 2601, Australia*
[3]*Cornell Center for Astrophysics and Planetary Science, Cornell University, Ithaca, New York 14853, USA*
[4]*Max Planck Institute for Gravitational Physics (Albert Einstein Institute), Am Mühlenberg 1, D-14476 Potsdam, Germany*

We propose two frequency-domain filters to analyze ringdown signals of binary black hole mergers. The first rational filter is constructed based on a set of (arbitrary) quasinormal modes (QNMs) of the remnant black holes, whereas the second full filter comes from the transmissivity of the remnant black holes. The two filters can remove corresponding QNMs from original time-domain ringdowns, while changing early inspiral signals in a trivial way—merely a time and phase shift. After filtering out dominant QNMs we can visualize the existence of various subdominant effects. For example, by applying our filters to a GW150914-like numerical relativity (NR) waveform, we find second-order effects in the $(l = 4, m = 4), (l = 5, m = 4)$, and $(l = 5, m = 5)$ harmonics; the spherical-spheroidal mixing mode in the $(l = 2, m = 2)$ harmonic; and a mixing mode in the $(l = 2, m = 1)$ harmonic due to a gravitational recoil. In another NR simulation where two component spins are antialigned with the orbital angular momentum we also find retrograde modes. The filters are sensitive to the remnant properties (i.e., mass and spin) and thus have a potential application to future data analyses and parameter estimations. We also investigate the stability of the full filter. Its connection to the instability of QNM spectra is discussed.

I. INTRODUCTION

Ringdown is the final stage of a gravitational wave (GW) signal emitted by a binary black hole (BBH) coalescence. It is associated with the oscillations of the remnant black hole (BH), and contains rich information of the system. With an increasing number of GW events [1–4] observed by ground-based detectors [5–7], comprehensive studies of the ringdown signal and its rich features become crucial to understanding the geometry of extreme spacetimes and testing General Relativity (GR).

A standard description of the ringdown comes from the BH perturbation (BHP) theory. The perturbation of a single BH has been an important topic for decades [8–11]. GWs emitted by the BH during ringdown are characterized by a set of quasinormal modes (QNMs),[1] which are complex and dissipative by their nature. As a consequence, the time-domain evolution of each QNM is a damped sinusoid. Due to the no-hair theorem [14–17], QNMs predicted by GR are completely determined by the mass and spin of the BH. Therefore, measuring the frequency and decay rate of a QNM from a ringdown signal would allow people to infer the mass and spin of the BH, as pointed out by Echeverria [18]. This method is dubbed *BH spectroscopy*. The idea was then generalized by Dreyer *et al.* [19] and Berti *et al.* [20,21], and they showed that one could test the no-hair theorem if multiple modes are observed at the same time. Subsequently, a lot of effort has been made to investigate BH spectroscopy under different scenarios [22–41]. In particular, the studies by Cardoso *et al.* [10,42,43], Foit *et al.* [44], and Laghi *et al.* [45] implied that QNMs could reflect the quantum nature of BHs or other exotic compact objects (ECOs); hence, one can use this fact to test GR and constrain modified gravity [46–49]. Since the detection of GW150914 [50], BH spectroscopy with real observational data has become available. Carullo *et al.* [51] studied the late-time portion of the ringdown of GW150914 and found no evidence for the presence of more than one QNM. Then Isi *et al.* [52] extended the analysis to the peak of the strain and showed evidence of at least one overtone, with 3.6σ confidence. This led to a test of the no-hair theorem at the

---

*[*]sma@caltech.edu
[1]Except for the late gravitational tail [12,13].

~20% level. Recently, Cotesta *et al.* [53] raised an opposing viewpoint that the search for the first overtone in the ringdown of GW150914 might be impacted by noises and therefore the conclusion still remains controversial [54,55]. On the other hand, Capano *et al.* [56] studied the QNM spectrum of GW190521 [57] and found the $l = m = 3$ harmonic. More GW events were used to perform BH spectroscopy in Refs. [58–60].

The inspiral-merger-ringdown (IMR) consistency test is another important extension of BH spectroscopy. One can infer the properties of binaries separately from the inspiral waves and the ringdown waves, and check whether they are consistent with the predictions of GR. The idea was proposed originally by Hughes *et al.* [61], and more careful analyses were carried out later [62–65]. So far, no deviation from GR has been found in observational data [66–69]. In addition, Refs. [70,71] used this method to test Hawking's area law [72].

An essential ingredient for BH spectroscopy is to understand how QNMs are excited at merger [73–86] and when the ringdown starts [87–89]. An accurate investigation for a BBH system during a highly nonlinear regime was not available until the numerical relativity (NR) breakthrough was made in 2005 by Pretorius [90]. Since then, a usual method to study the ringdown of a numerical waveform has been fitting it to the prediction of BHP theory. For example, Buonanno *et al.* [91] decomposed the ringdown signal into a sum of the fundamental mode and several overtones. Berti *et al.* [92,93] and Kamaretsos *et al.* [79] fit the ringdown of unequal-mass, nonspinning systems with only the fundamental mode. London *et al.* [94] carried out a more systematic study for various nonspinning BBHs and identified overtones within the NR waveforms. On the other hand, the fitting was also an important step to calibrate the effective one-body model [95–99]. Later, given the motivation of BH spectroscopy with real observational data, Thrane *et al.* [100] fit the ringdown of a GW150914-like NR simulation without any overtone, and they found some inconsistency between the QNM model (with fundamental modes only) and the NR waveform. This puzzle was resolved by Giesler *et al.* [101], where the authors found that the inclusion of overtones could extend the linear regime to the peak strain amplitude. This work sparked another wave for ringdown modeling, including the study for multimode-ringdown fitting [102], and the impacts of other effects on ringdown signals, such as retrograde modes[2] [103], more overtones [104], precessing systems [105], angular emission patterns [106], and the Bondi-van der Burg-Metzner-Sachs freedom [107].

It is surprising that the linear BHP theory is good enough to explain the waveform beyond the peak of the strain, given that the dynamics at the merger are believed to still be violent. Okounkova [89] provided a possible explanation based on previous Kerrness tests [87], most of the near-zone nonlinearities[3] are absorbed by the event horizon and barely escape to infinity. Nonetheless, it still seems elusive to draw an incontrovertible conclusion, since recent studies [110,111] showed that multipole moments of dynamical horizon are also compatible with the superposition of linear QNMs soon after the formation of the common horizon. Furthermore, it was shown that applying second-order BHP theory to the close-limit approximation could improve the agreement between the ringdown model and the full numerical waveform—the improvement was not only limited to the regime near the peak, but also extended to the late portion of the ringdown signal [112]. Then it is natural to ask *where are the second-order effects?* In the past, the second-order perturbation of a Schwarzschild BH was used by Tomita *et al.* [113,114] in the process of a gravitational collapse to investigate the stability of the horizon. Cunningham *et al.* [115] treated the spin as a small perturbation during the Oppenheimer-Snyder collapse and studied its second-order effect. Later on, second-order perturbation theory was motivated by the close-limit approximation [116], including the metric perturbation of a Schwarzschild BH [112,117–122] and the perturbation of a Kerr BH within the Newman-Penrose formalism [123]. Recently, more comprehensive treatments were used to deal with the perturbation of a Kerr BH and its metric reconstruction [124–126]. An important feature of second-order BHP theory is that the master equation has the same potential as the first-order theory, while the source term is quadratic in terms of the first-order perturbations. Accordingly, the time evolution of the second-order perturbations can be influenced by the second-order QNMs, known as "sum tones" and "difference tones" [127–131]. For instance, Nakano *et al.* [129] found the existence of a component twice the $(l = 2, m = 2)$ QNM in the $(l = 4, m = 4)$ harmonic by looking at a perturbed Schwarzschild BH. So far, very few studies have been done on the second-order effects within the ringdown of a BBH waveform. London *et al.* [94] investigated 68 NR waveforms and presented the evidence of the second-order mode $(l_1, m_1, n_1) \times (l_2, m_2, n_2) = (2, 2, 0) \times (2, 2, 0)$ in the $(l = 4, m = 4)$ harmonic via time-domain fitting. Beyond the second-order effect, Sberna *et al.* [132] showed that the growth of BH mass due to the absorption of the linear QNMs can induce a third-order secular effect.

The time-domain fitting proves to be powerful to extract the physics from ringdown signals. However, one always has to be careful of overfitting as including more QNMs (e.g., overtones or retrograde modes) may act as additional basis functions to misinterpret other effects. Taking this caveat into consideration, in this paper we propose a

---

[2]The author of Ref. [103] used the name "mirror mode" instead. In this work we will always use "retrograde mode".

[3]Here we do not consider the wave-zone nonlinearities, say the memory effect, which has been obtained from NR [108,109].

complementary tool to analyze a ringdown waveform; we define two frequency-domain filters that are able to remove any particular QNM from the ringdown. After the dominant mode is filtered out, we can visualize the existence of subdominant effects, including mode mixing, second-order modes, and retrograde modes.

This paper is organized as follows. In Sec. II we introduce two types of filters and show their properties. Then in Sec. III we apply the two filters to NR waveforms and discuss the results. Section IV focuses on the stability of the filter under perturbations. Next, in Sec. V, we discuss how the filter depends on the remnant BH's mass and spin. We also investigate the possibility to use the filter for parameter estimation. Finally, we summarize the results in Sec. VI.

Throughout this paper, we use the geometric units with $G = c = 1$. We always use the notation ω_{lmn} to refer to the (l, m, n) QNM.

II. QNM FILTERS

In this section we introduce two types of filters for QNMs. In Sec. II A we first review briefly the QNM decomposition model of a ringdown signal. Then in Sec. II B we describe a rational filter, which can remove any particular QNM from a ringdown signal. Two toy models are used to explore the effect of this filter. In Sec. II C, after understanding the effects of the rational filter, we argue that the inverse of the remnant BH's transmissivity can also serve as a filter. Remarkably, we find that the waveform filtered by this filter has a physical meaning.

A. Decomposing late waveforms into QNMs

It has been widely accepted that the late part of the GW emitted by binary black-hole mergers can be described as a linear combination of QNMs and a power-law tail, which arise from different features of the retarded gravitational Green's function G_{lm}; the QNMs correspond to poles of G_{lm}, while the power-law tail arises from integrating along a branch-cut G_{lm} [133].

In the special case of a high-mass ratio merger, which can be modeled as an orbiting and then plunging particle, QNM excitations at late times have been computed [77,78,80] and further analyzed in terms of multipole and overtone excitations [82,84,85,134]. As an example, in linear perturbation theory, the gravitational waveform at infinity sourced by the particle can be described by

$$h(t, r_*) = \sum_{lm} \int \frac{d\omega}{2\pi} e^{-i\omega t} \int dy \, G_{lm}(r_*, y, \omega) S_{lm}(y, \omega), \quad (1)$$

where $S_{lm}(y, \omega)$ is the source term, and it has the general form of

$$S_{lm}(y, \omega) = e^{i\omega T(y)} P(\omega, y), \quad (2)$$

where $(T(y), y)$ parametrizes the radial trajectory of the particle, and $P(\omega, y)$ is a rational function of ω. For each y, as long at $t > T(y)$ one can close the ω-contour from the lower-half complex plane, hence only collect the poles of the Green's function G_{lm} and a branch-cut contribution which corresponds to power-law tails. Even though the particle's $T(y)$ becomes infinity for $y \to -\infty$, the source term $P(\omega, y)$ exponentially decays to zero, soon after y becomes negative, i.e., when the particle plunges across the light ring and approaches the horizon.

Gravitational waveforms from collapsing stars and merging comparable-mass BHs were argued to have similar late-stage properties [18,115,135–139]. The regime of QNM decomposition is often referred to as the "linear regime", although the decomposition requires both linearity and homogeneity (i.e., the QNMs are homogeneous solutions to the linearized Einstein's equations).

Now assuming that a ringdown signal $h(\theta, \phi, t)$ is a linear combination of QNMs, starting from t_0, namely

$$h(\theta, \phi, t) = (h_+ - ih_\times)(\theta, \phi, t)$$
$$= \sum_{kmn} [A_{kmn} e^{-i\omega_{kmn}(t-t_0)}{}_{-2}S_{kmn}(a\omega_{kmn}, \theta, \phi)$$
$$+ A'_{kmn} e^{i\omega^*_{kmn}(t-t_0)}{}_{-2}S^*_{kmn}(a\omega_{kmn}, \pi - \theta, \phi)], \quad (3)$$

where $\times, +$ refer to two polarization states of the GW, a is the dimensional spin of the BH, ω_{kmn} are the frequencies of QNMs, ${}_{-2}S_{kmn}(a\omega_{kmn}, \theta, \phi)$ are the spin-weighted spheroidal harmonics [140], and (A_{kmn}, A'_{kmn}) are the mode amplitudes. It is usually more convenient to decompose the waveform in terms of spin-weighted spherical harmonics ${}_{-2}Y_{lm}(\theta, \phi)$

$$h(\theta, \phi, t) = \sum_{lm} h_{lm}(t){}_{-2}Y_{lm}(\theta, \phi), \quad (4)$$

with h_{lm} being the (l, m) spherical multipole harmonic. The mode mixing between the two bases, ${}_{-2}S_{kmn}(a\omega_{lmn}, \theta, \phi)$ and ${}_{-2}Y_{lm}(\theta, \phi)$, is given by [141,142]

$$_{-2}S_{kmn}(a\omega_{lmn}, \theta, \phi) = \sum_l \mu^*_{mlkn}(a\omega_{lmn}){}_{-2}Y_{lm}(\theta, \phi). \quad (5)$$

By combining Eqs. (3), (4), and (5), we obtain the QNM decomposition model for h_{lm},

$$h_{lm} = \sum_{k,n} [C_{mlkn} e^{-i\omega_{kmn}(t-t_0)} + C'_{mlkn} e^{i\omega^*_{k-mn}(t-t_0)}]. \quad (6)$$

Explicit relations between C_{mlkn} and A_{kmn} [Eq. (3)] can be found in Ref. [85]. Note that the second term in Eq. (6)

corresponds to the retrograde modes, which are also dubbed "mirror modes" in Refs. [103,143].

B. The rational filter and two toy models

For simplicity's sake we consider a single QNM signal in the time domain,

$$h(t) = e^{-i\omega_{lmn}(t-t_0)}\Theta(t - t_0), \tag{7}$$

where ω_{lmn} is the complex frequency of a specific QNM, $\Theta(t - t_0)$ is the Heaviside step function, and t_0 refers to the start time of the mode. If we are interested in the regime of $t > t_0$ and want to annihilate the mode content ω_{lmn} therein, a natural choice is to use a time-domain operator

$$\left(\frac{d}{dt} + i\omega_{lmn}\right)h(t) = \delta(t - t_0), \tag{8}$$

with $\delta(t - t_0)$ being the Dirac function. However, this operation can lead to additional numerical noises. Instead, we first transform the signal $h(t)$ in Eq. (7) to the frequency domain

$$\tilde{h}(\omega) = \frac{1}{\sqrt{2\pi}}\int h(t)e^{i\omega t}dt, \tag{9}$$

and obtain

$$\tilde{h}(\omega) = \frac{i}{\sqrt{2\pi}}\frac{e^{i\omega t_0}}{\omega - \omega_{lmn}}. \tag{10}$$

Then we define a frequency-domain filter $\mathcal{F}_{lmn}$,

$$\mathcal{F}_{lmn} = \frac{\omega - \omega_{lmn}}{\omega - \omega^*_{lmn}}, \tag{11}$$

where $*$ represents the complex conjugate. We remark that the numerator of $\mathcal{F}_{lmn}$ corresponds to the annihilation operator [Eq. (8)] in the frequency domain, while the denominator is introduced to make $|\mathcal{F}_{lmn}| = 1$ (when ω is real valued) and therefore ensures that the filter does not diverge at high frequency. Finally, we impose the filter via

$$\tilde{h}^{\text{filter}}(\omega) = \mathcal{F}_{lmn}\tilde{h}(\omega), \tag{12}$$

and transform the filtered signal to the time domain again

$$h^{\text{filter}}(t) = \frac{1}{\sqrt{2\pi}}\int \tilde{h}^{\text{filter}}(\omega)e^{-i\omega t}d\omega, \tag{13}$$

which yields

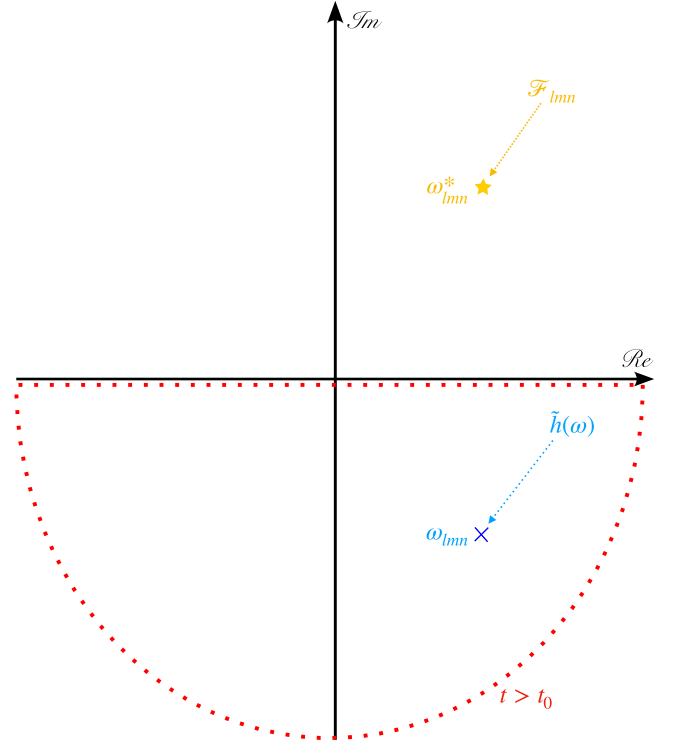$$h^{\text{filter}}(t) = -e^{-i\omega^*_{lmn}(t-t_0)}\Theta(t_0 - t). \tag{14}$$

FIG. 1. The pole of the original waveform $\tilde{h}(\omega)$ (in blue) and the filtered one $\tilde{h}^{\text{filter}}(\omega)$ (in orange). The contour is closed from the upper (lower) plane when $t < t_0$ ($t > t_0$).

Notice that the sign of the argument in the Heaviside step function Θ has changed. This can be understood in terms of the impact of the filter on the pole of the waveform, as shown in Fig. 1. The pole of the original waveform $\tilde{h}(\omega)$ (in blue) lies in the lower-half plane, implying its excitation after t_0. After imposing the rational filter $\mathcal{F}_{lmn}$, the pole is lifted to the upper panel (in orange). Therefore, the filtered waveform becomes a ring-up signal prior to t_0, whereas the original ringdown is removed after that moment.

To be specific, we consider a toy model in Fig. 2 to illustrate the effect of the filter. We pick the fundamental $(l = 2, m = 2)$ QNM of a Kerr BH with dimensionless spin $\chi = 0.69$. The QNM frequencies are obtained from the PYTHON package qnm [144]. The start time t_0 is set to 0. Indeed, we can see that within our interested regime $t > t_0$, the filter is able to remove the mode content ω_{lmn} completely. Meanwhile, the ring-up signal ("flipped ringdown") is introduced before t_0. As we will see, this feature can contaminate GWs at merger, but it will not affect our analysis as long as we focus on the regime $t > t_0$. As for an early, low-frequency inspiral signal, since its frequency ω is small compared to ω_{lmn}, we can perform a Taylor expansion around $\omega = 0$

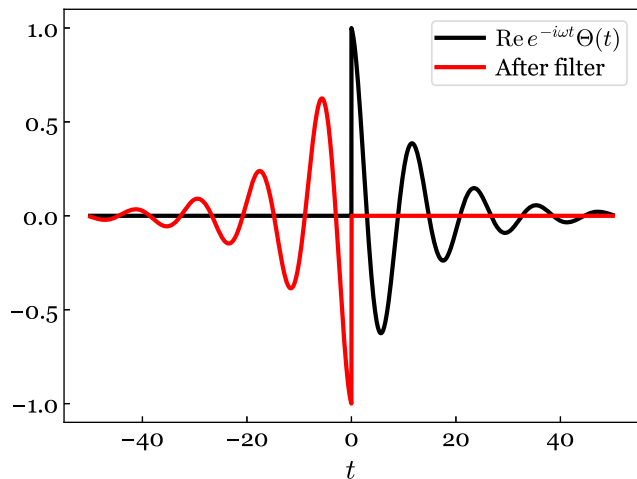$$\mathcal{F}_{lmn} = \exp[-i\phi_{lmn} - i\omega t_{lmn} + \mathcal{O}(\omega^2)], \tag{15}$$

FIG. 2. The effect of the frequency-domain filter in Eq. (11) on a single QNM signal. The mode is chosen to be the fundamental $(l = 2, m = 2)$ QNM of a Kerr BH with dimensionless spin 0.69. The signal starts at $t = 0$, and it is padded with 0 for $t < 0$. After applying the filter, the original signal (its real part is shown as the black curve) is removed from the regime of interest $(t > 0)$, whereas an undesired "flipped ringdown" is introduced for $t < 0$ (red curve). This "flipped ringdown" resembles the original signal, but decays backwards in time.

where the two real constants t_{lmn} and ϕ_{lmn} are given by

$$\phi_{lmn} = -2\tan^{-1}\frac{\omega^{\mathrm{i}}_{lmn}}{\omega^{\mathrm{r}}_{lmn}}, \qquad t_{lmn} = -\frac{2\omega^{\mathrm{i}}_{lmn}}{|\omega_{lmn}|^2}, \quad (16)$$

with $\omega^{\mathrm{r}}_{lmn}$ and $\omega^{\mathrm{i}}_{lmn}$ being the real and imaginary part of $\omega_{lmn} = \omega^{\mathrm{r}}_{lmn} + i\omega^{\mathrm{i}}_{lmn}$, respectively. Consequently, imposing the filter $\mathcal{F}_{lmn}$ to the low-frequency inspiral signal is equivalent to shifting the original signal in phase and backward in time.[4] For a Kerr BH with $\chi = 0.69$, the $(l = 2, m = 2)$ fundamental mode leads to $t_{lmn} \sim 0.57 M_f$, which can be neglected for most of ringdown analyses. However, if we want to remove a series of QNMs, we need to apply

$$\mathcal{F}_{\mathrm{tot}} = \prod_{lmn}\mathcal{F}_{lmn}, \qquad (17)$$

where n stands for the overtone index. Then the time shift t_{lmn} may not be negligible anymore.

We then switch our attention to a more realistic case; a Schwarzschild BH perturbed by an even-parity Gaussian pulse. The Zerilli equation [145] is solved numerically. Figure 3 shows the waveform h_{22} at future null infinity. We see h_{22} (the black curve) consists of the excitation, ringdown, and tail regime. After applying the filter $\mathcal{F}_{220}$ (the

<hr/>

[4]Strictly speaking, Eq. (16) is for zero frequency components. An accurate estimation for other low frequencies is not needed in this paper.
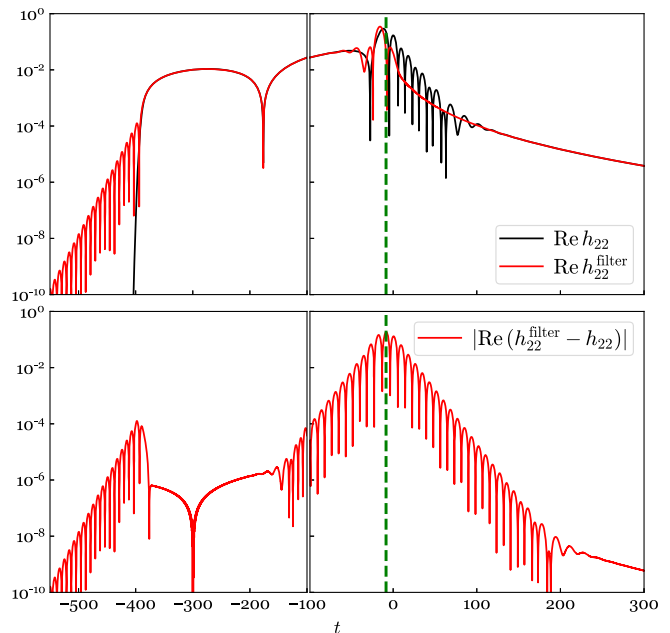

FIG. 3. The impact of the filter $\mathcal{F}_{220}$ on the GW emitted by a single, perturbed Schwarzschild BH. In the upper panel, the real part of the filtered waveform (red curve) is compared with the original h_{22} (black curve). Note that here we have undone the time shift induced by the filter by aligning two waveforms in the early regime. In the lower panel, the difference between the two waveforms corresponds to the combination of the "flipped ringdown" and the real ringdown (see the black and red curves in Fig. 2). Its peak (the vertical dashed line) represents the start time of the ringdown.

red curve), the ringdown oscillations are completely removed from the tail beyond a certain time around the merger, yet a few wiggles appear prior to that time. This is due to the nonphysical "flipped ringdown" (see the red curve in Fig. 2). The difference between the original h_{22} and the filtered waveform, as shown in the lower panel of Fig. 3, corresponds to the combination of the "flipped ringdown" and the real ringdown (namely the combination of the black and red curves in Fig. 2). Note that here we have undone the time shift induced by the filter by aligning two waveforms in the early regime. The peak of the difference (the vertical green dashed line) represents the start time of the ringdown t_0 [see Eq. (7)]. In addition, we see a generic feature; a new damped sinusoid that decays backward in time shows up before the onset of the original signal. For a BBH waveform, it appears before the entire inspiral regime, thus it does not impact our analysis.

C. The full filter: The inverse of BH transmissivity

Following Teukolsky's approach for the linear perturbation of a Kerr BH with dimensional spin a [146,147], we first write
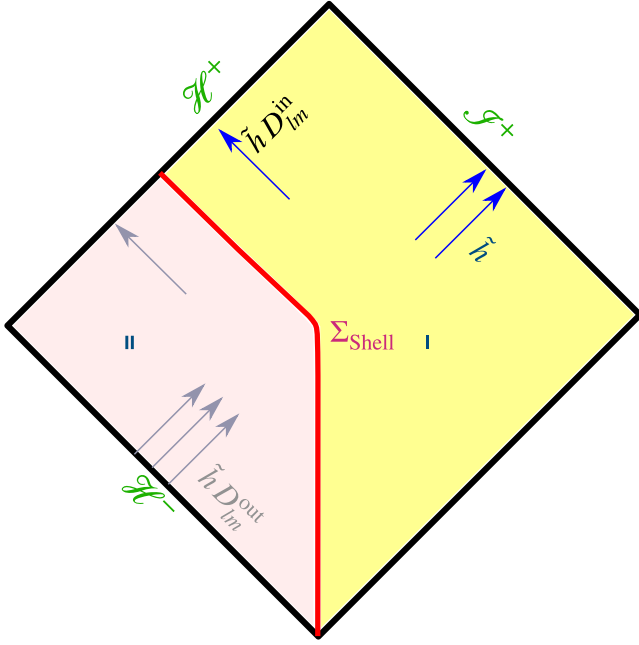
FIG. 4. The physical meaning of $\mathcal{F}^D_{lm}$ based on the hybrid approach. The spacetime is split by a timelike world tube Σ_{Shell} (red line) into an inner PN regime II and an outer BHP regime I. During the spacetime reconstruction, we take a waveform from NR at null infinity $\mathcal{I}^+$, and evolve it backwards into the bulk using BHP theory as if Σ_{Shell} were not there. The result is proportional to the up-mode solution to the homogeneous Teukolsky equation. In particular, an image wave $\tilde{h}D^{\text{out}}_{lm}$ needs to appear at the past horizon $\mathcal{H}^-$, and it is proportional to the filtered waveform. The image wave is spurious since the entire $\mathcal{H}^-$ lies inside the PN regime II, where the BHP theory does not apply. It exists there as a source to drive the wave in regime I. During the ringdown phase of $\tilde{h}$, the linear QNMs are free ringing of the remnant BH and hence can be annihilated by D^{out}_{lm}, whereas nonlinear pieces are driven by some sources and thus cannot be removed.

$$\Psi = \rho^{-4}\psi_4 = R_{lm}(r,\omega)_{-2}S_{lm}(a\omega,\theta,\phi)e^{i\omega t}, \quad (18)$$

where $\rho = -(r - ia\cos\theta)^{-1}$, (t,r,θ,ϕ) is the Boyer-Lindquist coordinate system, and ψ_4 is the Weyl scalar. The radial function $R_{lm}(r,\omega)$ satisfies the radial Teukolsky equation [146,147]. The up-mode solution R^{up}_{lm} to the homogeneous Teukolsky equation is of particular interest to us. Its asymptotic behavior near future null infinity and the horizon is given by [148]

$$R^{\text{up}}_{lm} \sim \begin{cases} r^3 e^{i\omega r_*}, & r_* \to +\infty, \\ D^{\text{out}}_{lm}e^{i\omega r_*} + \Delta^2 D^{\text{in}}_{lm}e^{-i\omega r_*}, & r_* \to -\infty, \end{cases} \quad (19)$$

with $\Delta = r^2 - 2r + a^2$ and r_* being the tortoise radius. Figure 4 exhibits the physical meaning of the up-mode—a wave is emitted from the past horizon $\mathcal{H}^-$ and it gets reflected and transmitted by the BH potential. The

transmissivity and reflectivity are given by $1/D^{\text{out}}_{lm}$ and $D^{\text{in}}_{lm}/D^{\text{out}}_{lm}$, respectively. As for a QNM of the BH, its mode frequency ω_{lmn} satisfies

$$D^{\text{out}}_{lm}(\omega_{lmn}) = 0. \quad (20)$$

Therefore, we can write

$$D^{\text{out}}_{lm} \sim \prod_n (\omega - \omega_{lmn}). \quad (21)$$

Comparing Eq. (21) with the filter in Eq. (17) [also Eq. (11)], we see D^{out}_{lm} serves the same role as $\mathcal{F}_{\text{tot}}$; it can remove all ω_{lmn}'s that are associated with the indices (l,m) at once. In practice, since D^{out}_{lm} diverges as $\omega \to 0$ [149], we instead define a filter

$$\mathcal{F}^D_{lm} = \frac{D^{\text{out}}_{lm}}{D^{\text{out}*}_{lm}}, \quad (22)$$

which is a direct analog of Eq. (11) to ensure $|\mathcal{F}^D_{lm}| = 1$ when ω is real valued. Below we will call $\mathcal{F}^D_{lm}$ the full filter.

Interestingly, unlike the filter in Eq. (11) that was introduced purely phenomenologically, the current filtered waveform $\tilde{h}D^{\text{out}}_{lm}$ bears a physical meaning. To be concrete, in Ref. [150], some use the hybrid approach [137,138] to reconstruct the spacetime near merging compact objects based on NR waveforms at future null infinity $\mathcal{I}^+$. Below we give a brief introduction and refer the interested readers to Refs. [137,138,150] for more details. The hybrid method is an approximated, *ab initio* waveform mode. For a BBH merger spacetime in Fig. 4, the spacetime is split by a timelike world tube Σ_{Shell} into an inner strong-gravity region II and an outer weak-gravity region I, where the strong-gravity metric in II is given by the post-Newtonian (PN) theory while the one in I is provided by BHP theory. The hybrid method evolves two metrics jointly and they communicate via boundary conditions on the world tube Σ_{Shell}. Note that close to the merger, the PN theory may break down, but the errors stay within the BH potential as long as the shell Σ_{Shell} falls rapidly enough into the future horizon $\mathcal{H}^+$. As a result, the hybrid method was able to predict a reasonable inspiral-merger-ringdown waveform for a BBH system [137,138].

In Ref. [150], on the other hand, we reversed the process —we started with a NR waveform at $\mathcal{I}^+$ and evolved it backward into the bulk (the region I) using BHP theory. This process allows us to construct the entire spacetime as if the world tube were not there. It turns out that the solution is proportional to the up-mode solution in Eq. (19), and the coefficient is determined by the NR waveform $\tilde{h}$ at $\mathcal{I}^+$. As shown in Fig. 4, the process leads to an outgoing wave $\tilde{h}D^{\text{out}}_{lm}$ at the past horizon $\mathcal{H}^-$, although it is not real because the entire $\mathcal{H}^-$ lies inside the strong-gravity region, where BHP theory does not apply. Nevertheless, we can think of

the filtered waveform $\tilde{h}D_{lm}^{\text{out}}$ as an image wave, which is akin to the image charge in electrodynamics. The image wave exists there to drive the signal in region I—acting as a source—by providing a desired boundary condition on Σ_{Shell}. In particular, during the ringdown phase of $\tilde{h}$, a linear QNM corresponds to the free ringing of the BH, and thus there is no corresponding source term. Consequently, it can be annihilated by D_{lm}^{out}, which is consistent with our phenomenological construction in Sec. II B. In contrast, second-order effects (during the ringdown phase) [117,125,126] are driven by sources, and hence cannot be removed by D_{lm}^{out}. The filtered waveform $\tilde{h}D_{lm}^{\text{out}}$ represents the image wave (an effective source) for the second-order effects.

III. APPLICATIONS OF THE FILTERS

In this section, we use three NR simulations, SXS: BBH:0305, 1107, and 1936, in the Simulating eXtreme Spacetimes (SXS) catalog [151] as examples to demonstrate the applications of the filters. As summarized in Table I, these three waveforms are for nonprecessing systems; the initial individual spins $\chi_{1,2}^{z}$ are (anti)aligned with the orbital angular momentum (along the z-axis), and the mass ratio between the primary BH and the secondary BH is denoted by q, i.e., $q > 1$. The systems undergo N_{cycle} quasicircular orbits before the merger. The remnants are Kerr BHs with mass M_f and spin χ_f. In particular, SXS: BBH:0305 is a GW150914-like system [50]. We want to emphasize again that our rational filter leads to a time shift backwards in time. For the sake of comparison, in this section we always undo the time shift by aligning the early portions of waveforms (i.e., minimizing their mismatch).

A. The GW150914-like system: SXS:BBH:0305

In this subsection, we investigate several (l, m) harmonics of SXS:BBH:0305. Section III A 1 focuses on h_{22}, where we show that the ω_{320} QNM mixes into h_{22} due to the spherical-spheroidal mixing [141,143,152]. Section III

TABLE I. A list of NR simulations (nonprecessing) used in this paper. The first column is the SXS identifier [151]. The second column is the mass ratio $q > 1$. The third column gives the number of quasicirular orbits that the systems undergo before the merger. The fourth and fifth columns correspond to the initial spin components along the direction of the orbital angular momentum (the z-axis). The remnant mass (M_f), as a fraction of the total system mass M_{tot}, and spin (χ_f) are in the final two columns. The waveform SXS:BBH:0305 is a GW150914-like system.

ID SXS:BBH:	q	N_{cycle}	χ_1^z	χ_2^z	$\frac{M_f}{M_{\text{tot}}}$	χ_f
0305	1.2	15.2	0.33	−0.44	0.952	0.692
1107	10.0	30.4	$\sim 10^{-6}$	$\sim 10^{-8}$	0.992	0.261
1936	4.0	16.5	−0.8	−0.8	0.985	0.022

A 2 focuses on second-order effects in h_{44}, h_{54}, and h_{55} contributed by the quadratic couplings h_{22}^2 and $h_{22}h_{33}$, respectively. Finally, in Sec. III A 3, we study the leakage of the ω_{220} mode into the harmonic h_{21} due to the gravitational recoil [152,153].

1. h_{22}: The spherical-spheroidal mixing

It was found that the harmonic h_{22} of SXS:BBH:0305 can be modeled as a superposition of $\omega_{22,n=0...7}$ up to the peak strain amplitude [101]. To compare our analysis results using the new method with theirs, we first apply a filter $\mathcal{F}_{l=2,m=2,n=0}$ [Eq. (11)] to h_{22}. As shown in Fig. 5, the filtered waveform (the red curve) has a smaller amplitude than h_{22} in the late ringdown regime, and we see that the main residual oscillation is consistent with the frequency and the decay rate of the first overtone ω_{221} (blue). Here the blue dashed curve is obtained by fitting the filtered waveform within the window of $[12, 28]M_f$; and the mode amplitude and phase of the first overtone are 0.08 rad and −0.57 rad at $t = 12M_f$. We note that the amplitude of the first overtone is reduced by $\mathcal{F}_{220}$ [154]. One needs to take the reduction factor into account while comparing with the original amplitude, and we leave this comparison for future work. On the other hand, the result serves as strong evidence to support that $\mathcal{F}_{lmn}$ is indeed able to annihilate the corresponding (l, m, n) QNM.

Next we continue to remove $\omega_{22,n=1...7}$ based on the conclusion in Ref. [101], and obtain the green curve in Fig. 5. We can see that the oscillation is consistent with ω_{320} (cyan) in the window of $[16, 65]M_f$, whose amplitude and phase are $\sim 4.4 \times 10^{-4}$ and −0.79 rad at $t = 16M_f$ after the filters. To ensure the oscillation is physical rather than numerical artifacts, we compute the numerical (truncation) error of this NR simulation by taking the difference between two adjacent numerical resolutions. We see that the residual in the filtered waveform is still above the numerical noise floor. Therefore, this piece of the dominant residual signal corresponds to the spherical-spheroidal mixing in the remnant Kerr spacetime[5] [141,143,152]. Meanwhile, we find the filter shifts the waveform backwards in time by $\sim 14.1M_f$, close to the prediction given by Eq. (16)

$$\sum_{n=0}^{n=7} t_{l=2,m=2,n} \sim 12.9 M_f. \tag{23}$$

In Fig. 5 we have aligned the early inspiral portion between the original signal h_{22} (the black curve) and the filtered waveforms for comparisons.

---

[5] The supertranslation can also make h_{32} leak into h_{22}, e.g., Eq. (8) of Ref. [152]. We have checked that the presence of the mode ω_{320} is due to the spherical-spheroidal mixing by transforming the waveform to the superrest frame using the technique presented in Ref. [155]. For more on this, see Ref. [107,155,156].
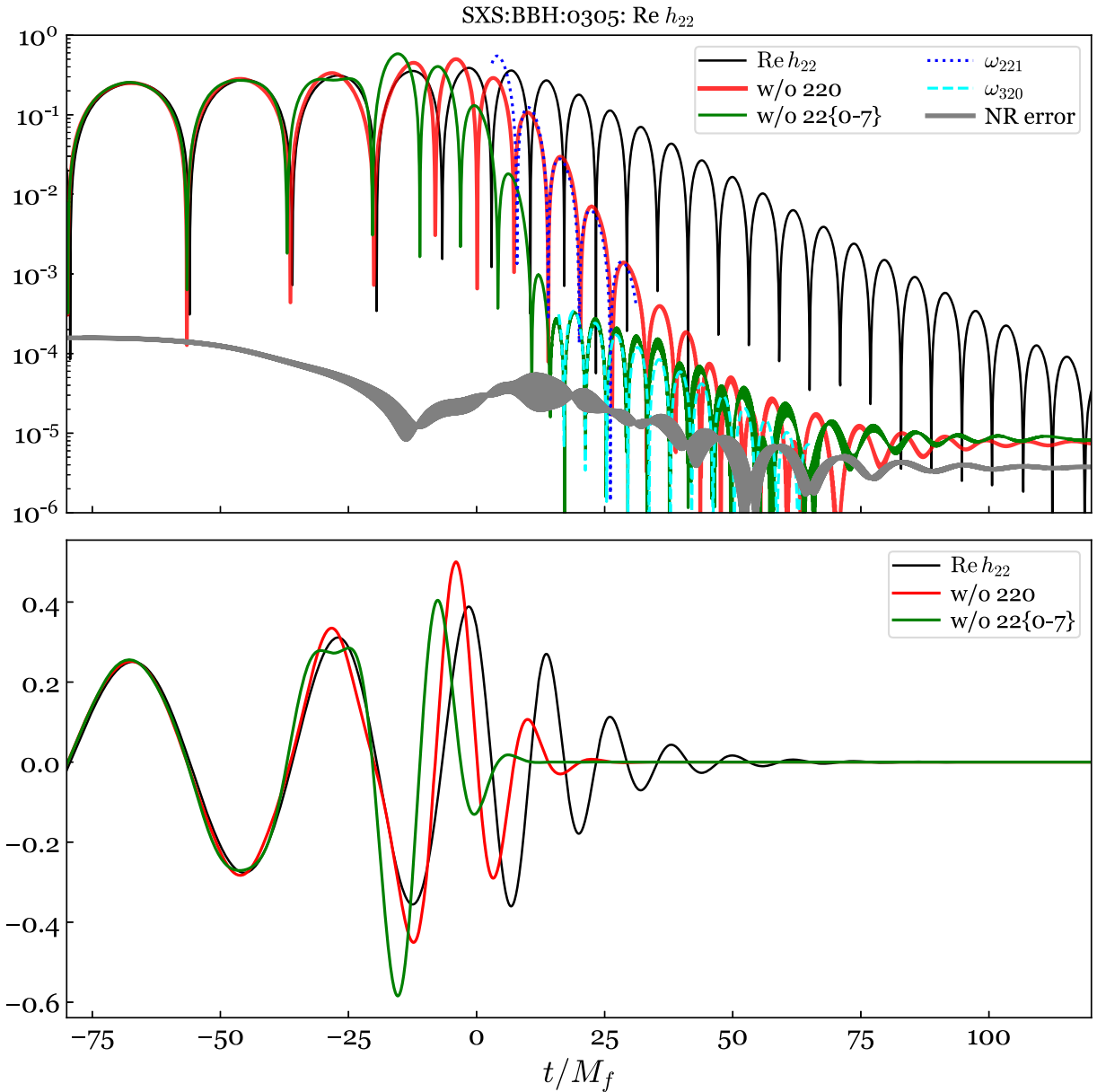
FIG. 5.   The effect of the filter $\mathcal{F}_{lmn}$ on h_{22} of SXS:BBH:0305. Here we have aligned the early inspiral portion between the original signal h_{22} (black) and the filtered waveforms. After removing ω_{220} from the original waveform, the oscillation in the ringdown of the filtered waveform (red) is consistent with the QNM ω_{221} (blue). If we further remove $\omega_{22,n=1...7}$, the residual shows the existence of the QNM ω_{320} (cyan), which is caused by the spherical-spheroidal mixing. For comparison, we evaluate the numerical error of this waveform (gray) by taking the difference between two adjacent numerical resolutions.

Then in Fig. 6 we investigate the effect of the full filter $\mathcal{F}^D_{lm}$ [Eq. (22)], where the value of D^{out}_{lm} is obtained from the Black Hole Perturbation Toolkit [157]. The result is almost identical to that of the rational filter $\mathcal{F}_{tot}$ up to $t \sim 10 M_f$, but it is less accurate to reveal the spherical-spheroidal mixing. We attribute the inaccuracy to the numerical noise when we interpolate the value of D^{out}_{lm} from the Black Hole Perturbation Toolkit, and we leave a more precise calculation of D^{out}_{lm} for future studies. In addition, we find a nice property of the full filter $\mathcal{F}^D_{lm}$; it does not give rise

to any time shift, as opposed to the rational filter. One could benefit from this feature in real data analyses.

2. h_{44}, h_{55}, h_{54}: The second-order QNMs

London *et al.* [94] found evidence for the second-order mode in the h_{44} harmonic, contributed by a quadratic coupling $\sim h^2_{22}$. Therefore, it is expected to see the sum tone $2\omega_{220}$ in the ringdown of h_{44}. In the upper panel of Fig. 7, we first remove the linear QNMs $\omega_{44,n=0...3}$ from h_{44}, and
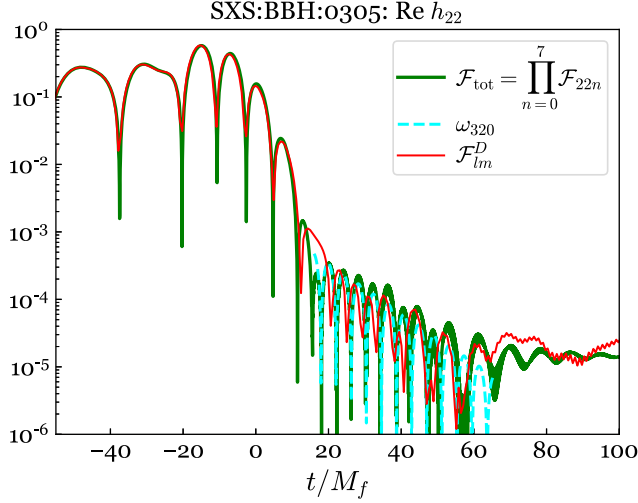
FIG. 6.   A comparison between the full filter $\mathcal{F}^D_{lm}$ [Eq. (22)] and the rational filter $\mathcal{F}_{\mathrm{tot}}$ [Eq. (17)] associated with $\omega_{22,n=0...7}$. The latter one is more accurate to reveal the existence of the QNM ω_{320} in h_{22} of SXS:BBH:0305. We attribute the inaccuracy of the full filter to the numerical noise when we interpolate the value of D^{out}_{lm} from the Black Hole Perturbation Toolkit.

then fit the filtered waveform with $2\omega_{220}$ in the window of $[12, 30]M_f$. We can see a decent agreement. The corresponding mode amplitude and phase are 7.9×10^{-4} and 3.1 rad at $t = 12M_f$ after the filters. In addition, the signal is larger than the numerical (truncation) error, which is evaluated by computing the difference between two adjacent numerical resolutions. This result shows that the second-order mode does exist in the ringdown regime. Furthermore, we find evidence for the presence of $\omega_{220} + \omega_{221}$ and $2\omega_{221}$ in the ringdown of h_{44} as well, and we leave more discussions in our follow-up work [158]. On the other hand, while we are preparing our manuscript, we notice that Ref. [159] also carries out comprehensive studies on the second-order modes with a different approach, so we refer the interested reader to Ref. [159] for more details.

In addition, it is also expected that h_{55}, h_{54} can be sourced by $h_{22}h_{33}$ and h^2_{22}, respectively. In this case, we find that one has to map the waveforms to the superrest frame [107,156] to reveal these second-order effects. We do this using the technique presented in Ref. [155], based on the SpECTRE code [160,161]. In the bottom left panel of Fig. 7, after removing the linear QNMs $\omega_{54,n=0...3}$, as well as $\omega_{44,n=0...3}$ and $\omega_{64,n=0...3}$ caused by the spherical-spheroidal mixing, we find the residual signal of h_{54} is consistent with the sum tone $2\omega_{220}$ in the window of $[10, 40]M_f$, with an amplitude of 1.2×10^{-5} and a phase of -2.9 rad at $t = 10M_f$. As for h_{55}, the bottom right panel of Fig. 7 shows the existence of $\omega_{220} + \omega_{330}$ in $[8, 28]M_f$, whose amplitude and phase are 1.9×10^{-5} and -1.96 rad at $t = 8M_f$. Nevertheless, we see the amplitudes of

these two second-order effects are on the same order of the numerical noise, therefore their existence is not conclusive.

Finally, we want to remark again that the amplitudes of the second-order effects are reduced by the filters. In consequence, the amplitudes obtained from our approach are smaller than their original values.

3. h_{21}: The mode mixing due to a gravitational recoil

We repeat our process for the harmonic h_{21} of SXS: BBH:0305. As shown in Fig. 8, after removing the linear QNMs $\omega_{21,n=0...2}$ and the spherical-spheroidal mixing modes $\omega_{31,n=0,1}$, we find the remaining oscillation is consistent with the mode ω_{220} (the red and yellow dashed curves). We then use ω_{220} to fit the filtered waveform in the window of $[55, 92]M_f$. The result is shown as the yellow dashed curves. The corresponding mode amplitude and phase are 9.5×10^{-6} and -0.62 rad at $t = 55M_f$. This leakage is caused by a boost in the orbital plane, and this phenomenon has been discussed by Kelly *et al.* [152] and Boyle [153]. To verify this, we transform the waveform to the superrest frame (the blue curve) [107,156], where the remnant BH is in the center-of-mass frame. After applying the same filter, we can see the mixing is completely removed (the green curve), while the other portion of the waveform remains unchanged.

We note that the leakage of ω_{220} into h_{21} is a common phenomenon, especially for high mass-ratio events whose kick velocities are relatively large. Failing to take this effect into account may misinterpret the mixing mode ω_{220} as retrograde modes [103,143]. We will explain more details in Sec. III B.

B. The retrograde modes

It was found that taking into account the retrograde modes [e.g., the second term of Eq. (6)] would expand the linear perturbation regime. To partially address the debate on overfitting, we use our rational filter as a complementary tool to visualize the presence of the retrograde modes.

We first take SXS:BBH:1936 with non-negligible retrograde modes (see Appendix A of Ref. [150]). In the top panel of Fig. 9, we remove the prograde modes $\omega_{22,n=0...3}$ and the spherical-spheroidal mixing mode ω_{320} from the original harmonic h_{22} (the black curve), then the red curve shows the existence of $-\omega^*_{2-20}$ in the residual. In the plot, the green dashed curve is obtained by fitting the filtered waveform with $-\omega^*_{2-20}$ in the window of $[28, 60]M_f$. Its mode amplitude and phase are 3.9×10^{-4} and 2.6 rad at $t = 28M_f$. To further support our result, we investigate the phase evolution of the waveforms. For a prograde mode, its phase should decrease monotonically over time due to the term $e^{-i\omega_{lmn}t}$ [see the first term of Eq. (6)], whereas a retrograde mode's phase should increase due to the term $e^{i\omega^*_{l-mn}t}$ [see the second term in Eq. (6)]. In the bottom panel
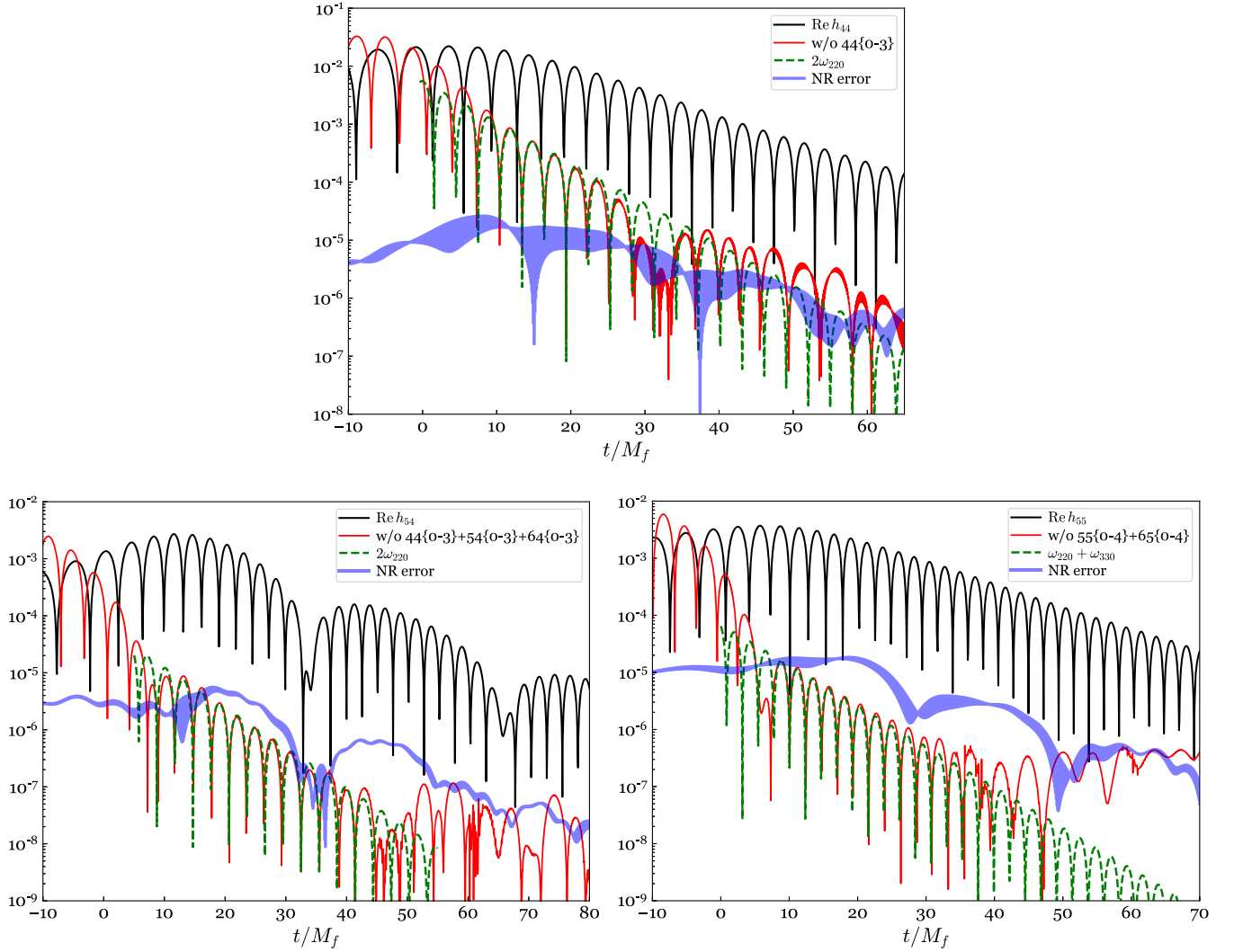
FIG. 7.   Second-order modes in h_{44} (top), h_{54} (bottom left), h_{55} (bottom right) of SXS:BBH:0305. After removing linear QNMs and relevant spherical-spheroidal mixing modes from original waveforms (black curves), filtered waveforms (red curves) contain oscillations that are consistent with the sum tone of $2\omega_{220}$ or $\omega_{220} + \omega_{330}$ (green dashed curves). As for the harmonics h_{55} and h_{54}, the comparison is done in the superrest frame to avoid other mixing modes.

of Fig. 9, we see the phase of the original waveform (the black curve) decreases with time, indicating that the progrades are more dominant. After applying the filter, the decreasing trend terminates at $\sim 16M_f$ after the peak and the phase starts to grow at the same time that the residual oscillations in the top panel appear. This observation confirms the physical origin of the residual oscillations.

Then we look into the case of SXS:BBH:1107 investigated by Dhani [103]. As shown in Fig. 10, there are a few cycles in the filtered residual waveform h_{22} (the red curve) that are consistent with the retrograde mode $-\omega_{2-20}^*$. Meanwhile, the phase of the filtered waveform also grows

within that regime, which serves as more evidence. Nevertheless, the retrograde mode in this case is weaker and noisier than that of SXS:BBH:1936. Furthermore, we find applying retrograde filters (not only the fundamental mode but also overtones) has little impact on the early portion ($t \lesssim 0$) of the red curve in Fig. 10, meaning there is no strong evidence for the existence of retrograde modes within that regime. As for the harmonic h_{21}, we find it has a mixing component from the mode ω_{220} due to the gravitational recoil, similar to the case discussed in Sec. III A 3. This effect was not taken into consideration by Dhani [103], so we speculate that this could be the cause for the crests and troughs in the mismatch of h_{21}, e.g., Fig. 3 of Ref. [103].
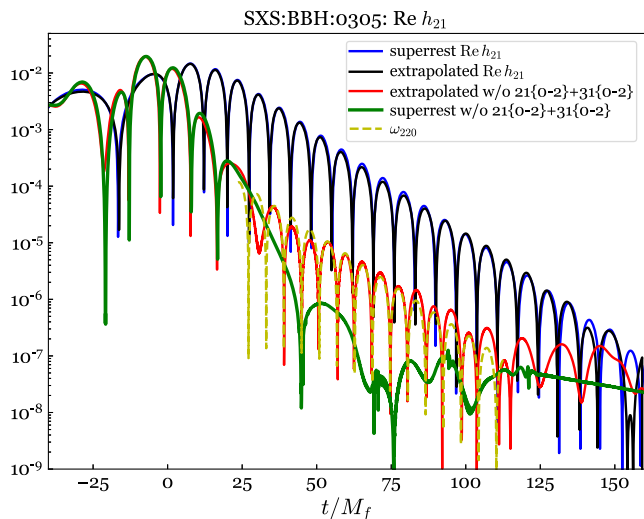
FIG. 8. Leakage of the ω_{220} mode into the h_{21} harmonic due to the gravitational recoil. After removing $\omega_{21,n=0\ldots2}$ and $\omega_{31,n=0,1}$ from the original h_{21} waveform (black curve), the red curve exhibits the presence of the ω_{220} mode (yellow dashed curve). If we transform the waveform to the superrest frame (blue curve) and repeat our filtering process, the mixing mode ω_{220} will be completely removed (green curve).

Finally, we want to note that the vertical dashed lines in Figs. 9 and 10 do not necessarily correspond to the start time of the retrograde mode $-\omega^*_{2-20}$ in the original waveforms (the black curves), because of the time shift induced by our rational filter. To undo the time shift, here we simply align the early inspiral portion of the filtered waveforms with the original ones, making the location of the dashed lines less informative.

IV. THE STABILITY OF THE FULL FILTER $\mathcal{F}^D_{lm}$

The QNM spectra of BHs have been found to be unstable [162–166]. In particular, Cheung *et al.* [166] classified the instability into two categories; "migration instability" and "overtaking instability". For migration instability, the fundamental QNM drifts drastically from its unperturbed value when the perturbation is distant from the BH. This kind of instability is related to the asymptotic behavior of the eigenfunction near the horizon $(e^{-i\omega_{lmn}r_*})$ and infinity $(e^{i\omega_{lmn}r_*})$. Recalling that $\mathrm{Im}\,\omega_{lmn} < 0$, the eigenfunction of the QNM increases exponentially as $|r_*| \to \infty$, any small perturbation of the BH potential at a large $|r_*|$ will lead to a significant change of ω_{lmn}. For overtaking instability, a family of new modes appears near a bumpy BH, trapped between two potential barriers.[6] One of the new modes might have a smaller decay rate than the unperturbed fundamental mode when the perturbation is at a large

---

[6]They are called "matter-driven" modes by Barausse *et al.* [163,164].
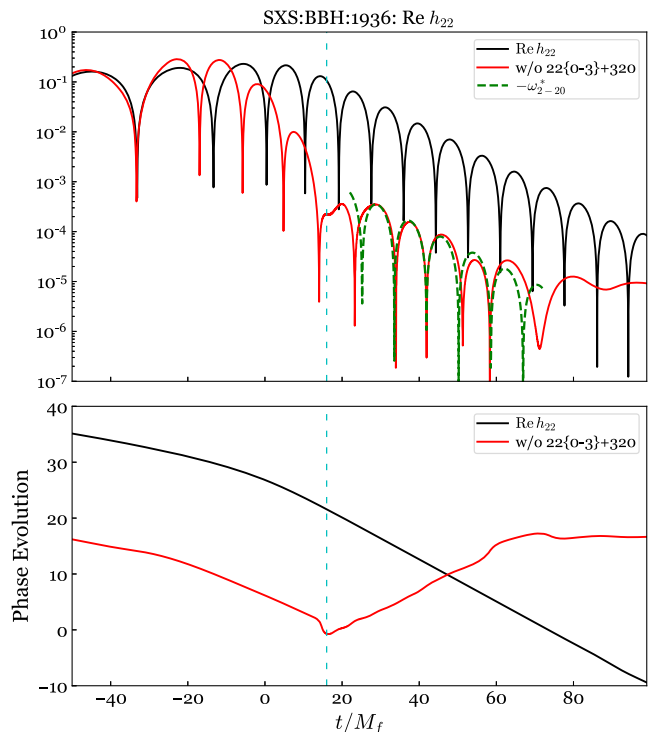

FIG. 9. Retrograde mode $-\omega^*_{2-20}$ in the ringdown of SXS: BBH:1936. Top panel: After removing the $\omega_{22,n=0\ldots3}$ modes and the spherical-spheroidal mixing mode ω_{320} from the original harmonic h_{22} (black curve), we reveal the presence of $-\omega^*_{2-20}$ (green dashed curve) in the residual waveform (red curve). Bottom panel: The phase evolution of the original waveform (black curve) and the filtered waveform (the red curve). The phase of the original waveform decreases monotonically, indicating that the prograde modes are dominant. However, the phase of the filtered waveform starts to grow at the same time as the residual oscillations in the top panel appear, which demonstrates that the residual oscillations are retrograde modes.

distance. Consequently, this new mode overtakes the original fundamental mode.

The spectral instability, however, may have a limited effect on observational results (e.g., time-domain responses of a BH), as discussed in Refs. [43,162–164,167,168]. Nollert [162] and Barausse *et al.* [163,164] showed that the prompt time-domain response is independent of perturbations when the perturbations are far from the system, even though the QNMs of the perturbed system are completely different from the ones of an isolated BH. Cardoso *et al.* [43] drew a similar conclusion while considering near-horizon perturbations. In fact, as pointed out by Hui *et al.* [169] and Berti *et al.* [167], despite the nonlocality of QNMs, one needs to appreciate the causal structure of the system while considering the time-domain signals—a time response reflects the nature of each single potential bump that is causally connected to the observer, e.g., the prompt ringdown of a regular BH. The QNMs of the perturbed system do not show up until very late times as "echoes" [170]
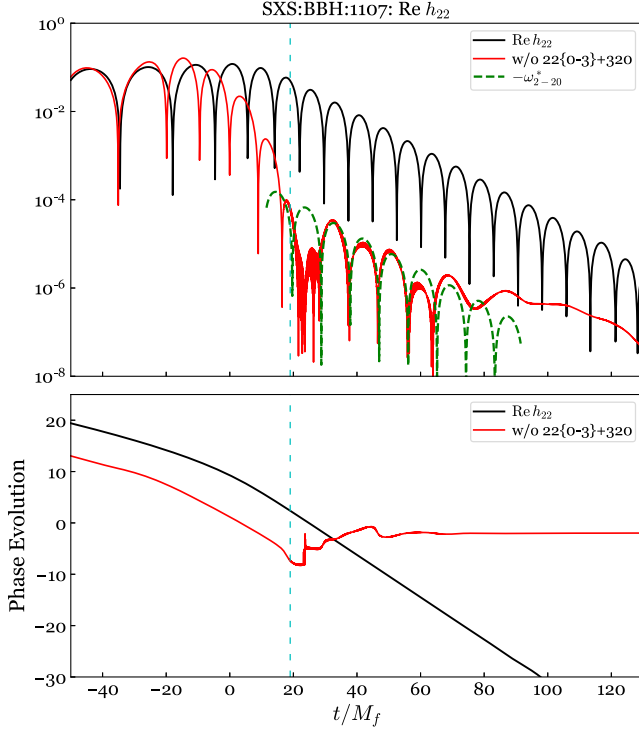
FIG. 10. Same as Fig. 9, the retrograde mode $-\omega_{2-20}^{*}$ in the h_{22} of SXS:BBH:1107.
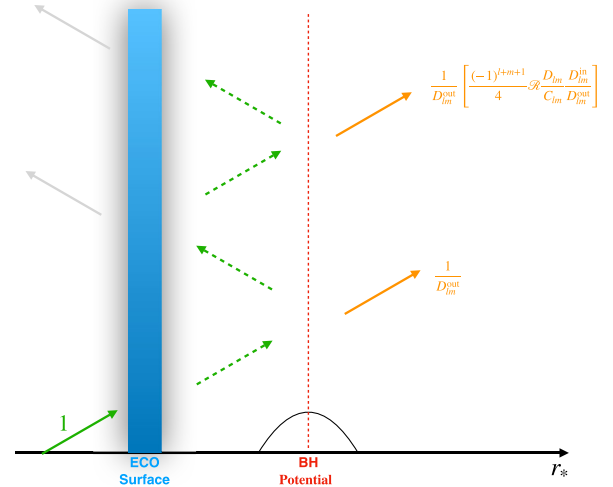

FIG. 11. The up-mode solution of an ECO. We assume that a GW emerges from the horizon ($r_* = -\infty$) and its amplitude is unity. It bounces back and forth within the cavity formed by the ECO surface and the BH potential. The GW seen by an observer at infinity consists of the main transmissive wave $1/D_{lm}^{\text{out}}$ and a series of echoes.

when the initial Cauchy data travels and experiences the entire potential.[7] Therefore, the time-domain signal is stable in the sense that the original waveform remains unchanged, whereas the additional perturbation appears only as echoes that are well separated from the original signal in time.

The instability of the QNM spectra implies that QNMs may not be the most natural basis for ringdowns. One might need to rearrange QNMs into new subsets and sum each subset to form a new basis, in either time or frequency domain. In fact, the backwards one-body (BOB) model [175] is an inspiring example, where the contributions of overtones associated with the same (l, m) harmonic are rearranged and summed into a single time-domain function $\sim \text{sech}\gamma t$, where γ is a constant. One may further postulate that the time-domain function could be treated as the leading term of a new set of basis and the term $\sim \text{sech}\gamma t$ provided by the BOB model contains most power of the ringdown. Another relevant time-domain basis was discussed by some of us for superkick systems [176]; it was found that the time-domain basis can even be extended to the inspiral regime for the superkick systems. A direct consequence is the collective

excitation of QNMs; the amplitudes of different QNMs are correlated as a result of the time-domain basis being projected to the QNM basis. In fact, such a correlation (universality) has been found in not only the superkick systems [176], but also extreme mass-ratio inspirals [82–85,134].

Based on the above discussions, we want to ask: Do the filters reflect the nature of the system? Can we distinguish a BH from other objects (e.g., a bumpy BH or an exotic compact object) using our filters? In particular, since the full filter $\mathcal{F}_{lm}^{D}$ contains a collection of the corresponding QNMs ω_{lmn}'s as a result of Eq. (21), is the filter stable or not under perturbations in the BH potential, given the spectral instability? In fact, a similar topic has been investigated recently by Kyutoku *et al.* [168]. The "phase shift" introduced by the authors is essentially the phase of our full filter in Eq. (22), and they showed that the phase shift of a Schwarzschild BH is stable when it is perturbed by a small Pöschl-Teller bump. In this work, we continue their studies and adopt another simple model to provide a qualitative answer. More sophisticated discussions are left for future work.

In Fig. 11, we consider an exotic compact object (ECO) whose surface is close to the would-be horizon. The surface can partially reflect GWs and the reflectivity $\mathcal{R}$ is given by

$$\mathcal{R} = \epsilon e^{-2ib}, \tag{24}$$

where ϵ is a constant, and $r_* = -b$ is the location of the ECO surface with the factor of two representing the round trip between the ECO surface and the BH potential. By imposing a physical boundary condition based on the

---

[7]We note that QNMs can become complete under some conditions [171–173] (see also Refs. [162,174] for relevant discussions). In particular, Beyer [171] showed the completeness of QNMs of the Poeschl-Teller potential at a late time—a regime where solutions can be expanded with respect to its QNMs.

membrane paradigm at the ECO surface [177], we obtain the up-mode solution [in parallel with Eq. (19)],

$$R_{lm}^{\mathrm{up\,ECO}} \sim \begin{cases} r^3 e^{i\omega r_*}, & r_* \to +\infty, \\ \tilde{D}_{lm}^{\mathrm{out}} e^{i\omega r_*} + \Delta^2 \tilde{D}_{lm}^{\mathrm{in}} e^{-i\omega r_*}, & r_* \to -\infty, \end{cases} \quad (25)$$

with

$$\tilde{D}_{lm}^{\mathrm{out}} = D_{lm}^{\mathrm{out}} \left[1 - (-1)^{l+m+1} \mathcal{R} \frac{D_{lm}}{4C_{lm}} \frac{D_{lm}^{\mathrm{in}}}{D_{lm}^{\mathrm{out}}} \right], \quad (26)$$

where the factor D_{lm}/C_{lm} comes from the Teukolsky-Starobinsky (TS) relation [148,178]. We refer interested readers to Appendix A for derivation. Note that Eq. (26) takes a similar form to the Wronskian in Eq. (5.2) of Ref. [169].

We then define the filter $\mathcal{F}_{lm}^{DECO}$ for the ECO system,

$$\mathcal{F}_{lm}^{DECO} = \frac{\tilde{D}_{lm}^{\mathrm{out}}}{\tilde{D}_{lm}^{\mathrm{out*}}}. \quad (27)$$

To transform the filter to the time domain, we first need to apply the Planck-taper filter $\mathcal{F}(\omega)$ [179] to remove the high-frequency contribution,

$$\mathcal{F}(\omega; \omega_1, \omega_1) = \begin{cases} 0, & \omega < \omega_1, \\ \frac{1}{e^z+1}, & \omega_1 < \omega < \omega_2, \\ 1, & \omega > \omega_2, \end{cases} \quad (28)$$

with

$$z = \frac{\omega_2 - \omega_1}{\omega - \omega_2} + \frac{\omega_2 - \omega_1}{\omega - \omega_1}. \quad (29)$$

Figure 12 shows a nonspinning ECO case. The filters for a spinning ECO have the same qualitative feature so we refer readers to Appendix B for results. In the absence of perturbations, we see that the black curve assembles the Dirac function $\delta(t)$ near $t = 0$ because of the fact that $|\mathcal{F}_{22}^{DECO}(\omega)| = 1$. Most of the signals (i.e., the damped sinusoids) lie on the left side of the Dirac function ($t < 0$), and the reason is exactly the same as the flipped ringdown in Fig. 2. We also see the tail-like feature at an earlier time.

Next, we turn to the perturbation. Since Cheung *et al.* [166] found the spectral instability with b varied, in Fig. 12a, we first compute the filter with two choices of b, while fixing $\epsilon = 0.1$. We find the modification to the original signal is negligible. The major change is a series of echoes with an interval of $\Delta t \sim 2b$—well separated from the original signal (in the plot we only show the first one or two echoes). Meanwhile the amplitude of the echo is

independent of b. We remark that the δ function is removed from echoes since the TS coefficient $|D_{lm}/C_{lm}| \to 0$ as $\omega \to \infty$. Then in Fig. 12b, we fix the value of b to $200M_f$ but vary ϵ. Again, the perturbation has little impact on the original signal, and the amplitude of the echo scales linearly with ϵ. Compared to the recent work by Berti *et al.* [167], our studies include not only the fundamental mode, as Berti *et al.* [167] did, but also more overtones. Nevertheless, the qualitative features in our results are the same as theirs. Finally, Fig. 13 shows the real part of $\mathcal{F}_{22}^{DECO}(\omega)$ in the frequency domain for completeness.

V. INFERRING REMNANT PROPERTIES FROM THE RATIONAL FILTER

We have shown that our rational filter $\mathcal{F}_{lmn}$ is able to remove a specific QNM ω_{lmn} from the ringdown regime and reduce the root sum square (RSS) of the ringdown. In particular, the ringdown signal can be almost completely removed if we apply a filter with a series of corresponding modes. Since the mode frequencies ω_{lmn} are determined by the mass M_f and spin χ_f of the remnant BH, in this section, we investigate how the ringdown RSS decreases depending on the choices of M_f and χ_f.

We define the RSS of a filtered harmonic $h_{lm}^f(t)$ within a time interval $[t_0, t_1]$ to be

$$\mathrm{RSS} = \sqrt{\int_{t_0}^{t_1} |h_{lm}^f(t)|^2 dt}. \quad (30)$$

We still take the GW150914-like waveform SXS: BBH:0305 as an example. We fix t_1 to $100M_f$ and let t_0 vary. Then we apply a filter,

$$\mathcal{F}_N(M_f, \chi_f) = \mathcal{F}_{320}(M_f, \chi_f) \prod_{n=0}^{N} \mathcal{F}_{22n}(M_f, \chi_f), \quad (31)$$

to the harmonic h_{22}. The filter $\mathcal{F}_N$ is a function of remnant mass M_f and spin χ_f. It also depends on how many ($l = 2$, $m = 2$) overtones we want to remove. We want to emphasize that our rational filter leads to a time shift, and in Sec. III we undid it by aligning early inspiral waveforms. However, in this case we find the alignment can pull some nonringdown signals into the regime that we are interested in ($t > t_0$) and make our analyses fail. To avoid this, here we do not perform this alignment. A caveat of this compromise is that the time shift itself can reduce the RSS, even though it is a subdominant effect. In this paper, we ignore the contribution due to this time shift, and leave more self-contained studies for future work.

In Fig. 14, we vary the value of χ_f with different choices of N and t_0 while keeping M_f fixed at the true value. When
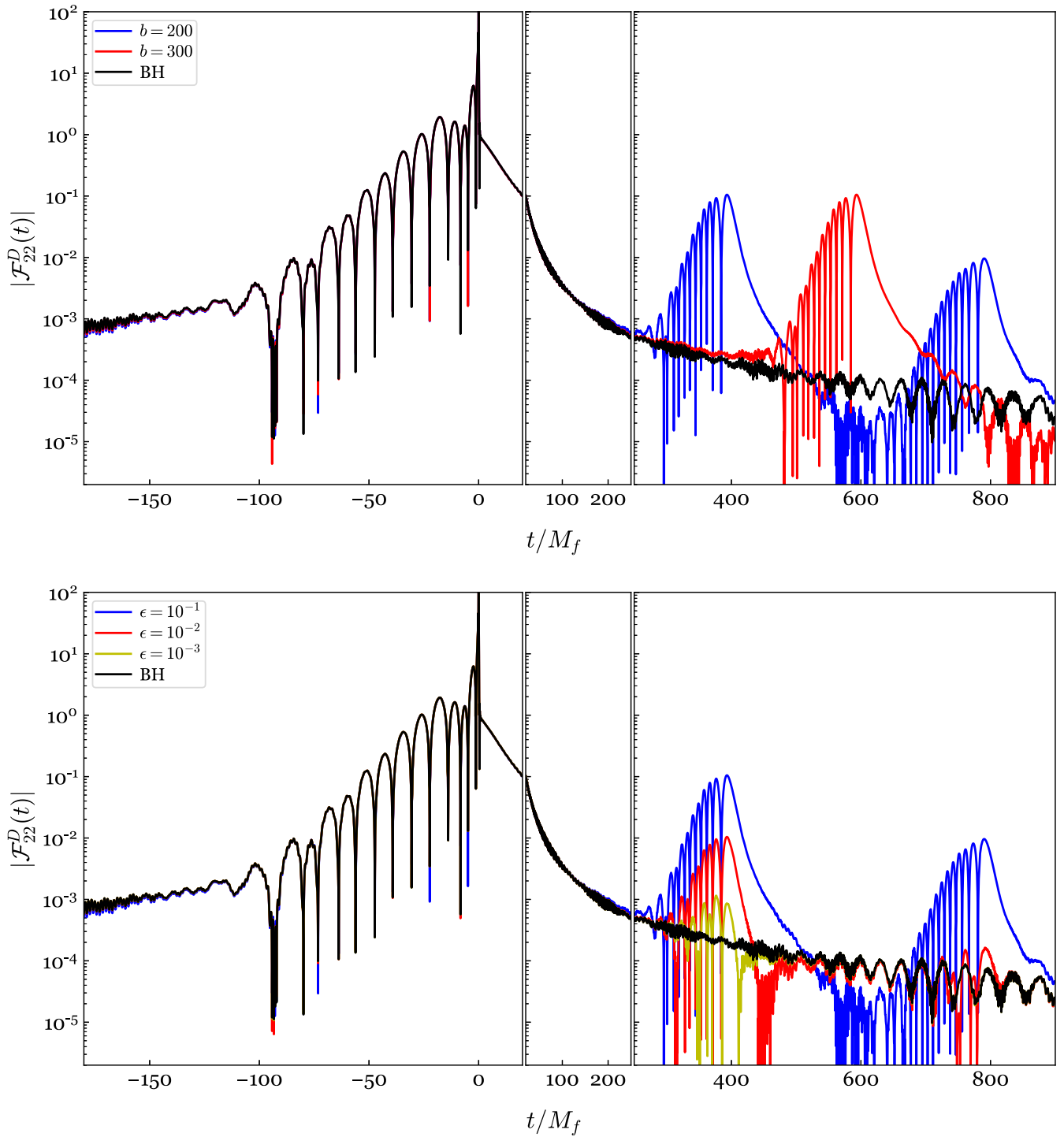
FIG. 12.   The filter $\mathcal{F}_{lm}^{\mathrm{DECO}}$ of a nonspinning ECO in the time domain. In the top panel, we set b to $200M_f$ (blue) and $300M_f$ (red), while fixing the value of ϵ to 10^{-1}. They are compared with that of a Schwarzschild BH (black). In the bottom panel, we choose $\epsilon = 10^{-1}, 10^{-2}, 10^{-3}$ (blue, red, and yellow) and set b to $200M_f$. In both cases, the original signal (around $t \sim 0$) remains unchanged. The perturbation appears as periodic echoes with the time interval $2b$. The amplitude of the nth echo is proportional to ϵ^n.
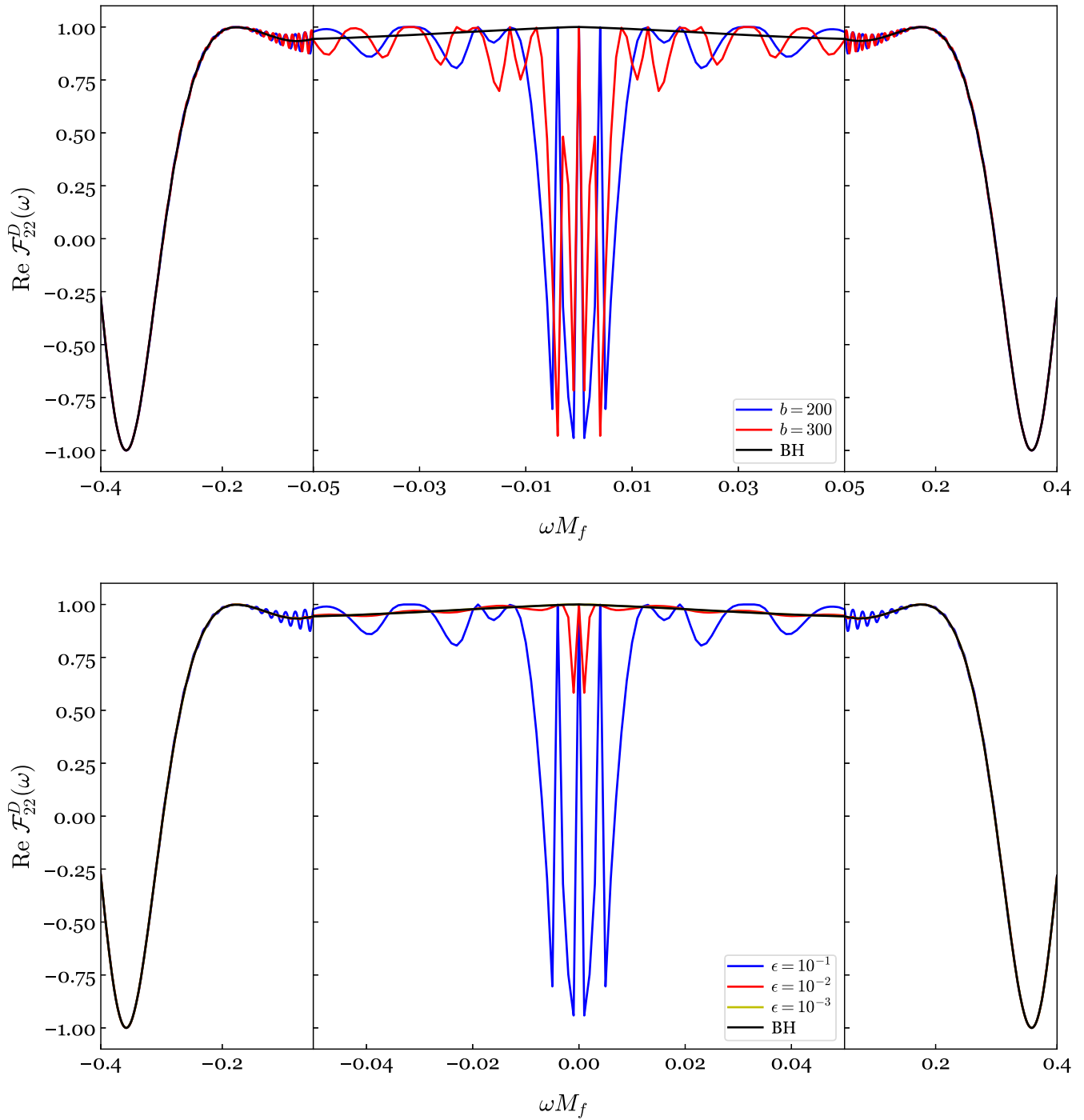
FIG. 13.   Same as Fig. 12. The real part of $\mathcal{F}_{22}^{D}$ in the frequency domain.

t_0 is large ($\sim 50 M_f$), we see the true value $\chi_f^{\text{true}} = 0.692$ leads to the smallest RSS (namely the ringdown is mostly removed) regardless of the value of N. This is because in the regime of $t \gtrsim 50 M_f$, the signal is dominated by the fundamental mode ω_{220}, and removing ω_{220} alone is

enough to reduce the RSS down to roughly the numerical noise level. However, if we push t_0 to an early time, failing to filter out enough modes will result in incorrect values of χ_f when RSS achieves its local minimum; the value χ_f is degenerate with the choice of t_0. Especially, in the first
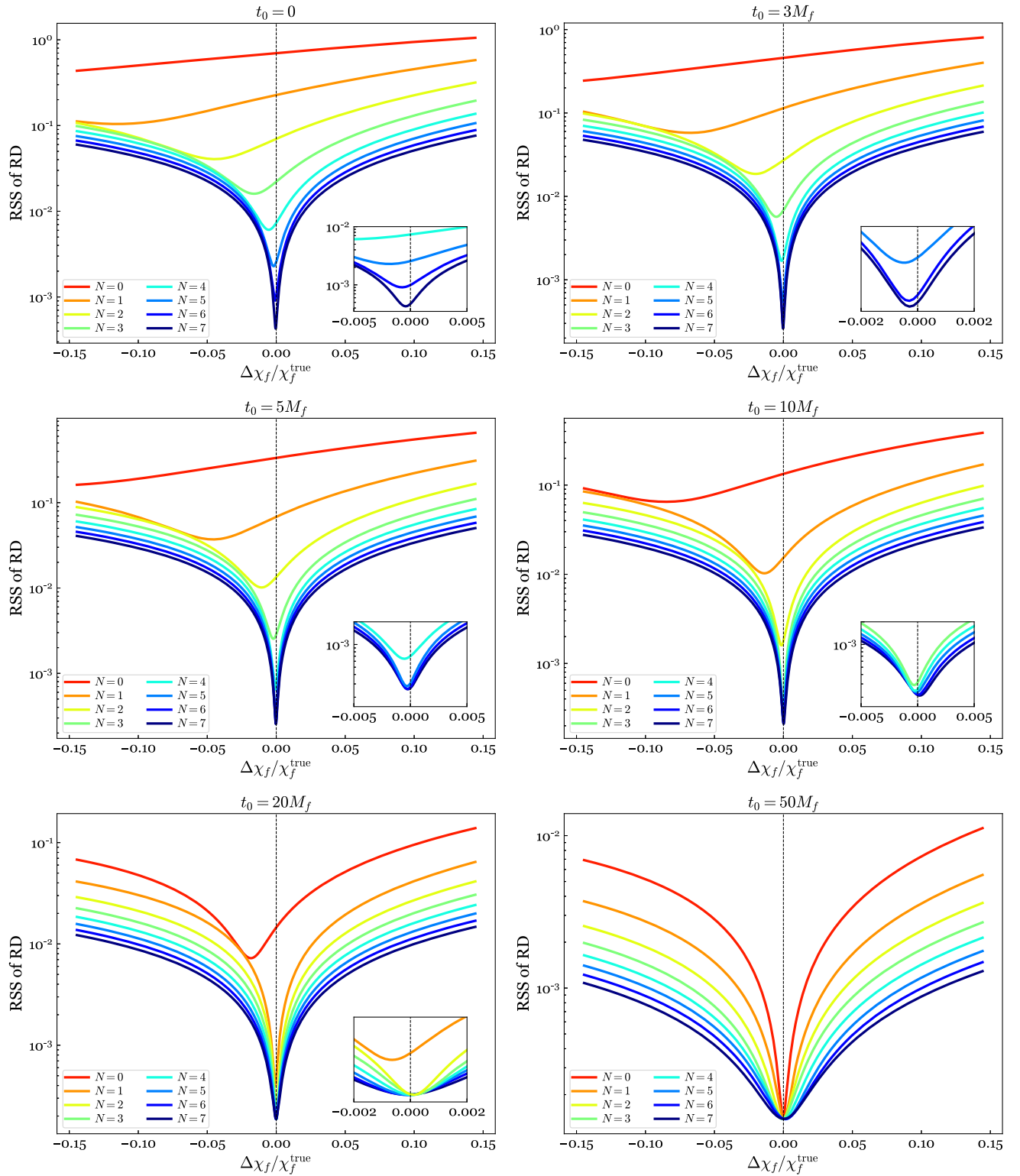
FIG. 14. The ringdown RSS of the filtered waveform as a function of χ_f. The SXS:BBH:0305 waveform is used. The six panels correspond to different choices of the start time, i.e., t_0 in Eq. (30). In each panel, different colors indicate the results from removing different numbers of overtones. When t_0 is large ($\sim 50 M_f$), the true value of the spin $\chi_f^{\text{true}} = 0.692$ leads to the smallest RSS no matter how many overtones are removed. However, if we push t_0 to an early time, enough overtones need to be removed to obtain the true value. On the other hand, the RSS depends strongly on χ_f; a 2% change in χ_f can result in around two orders of magnitude change in the RSS, when t_0 and N are fixed to their true values.
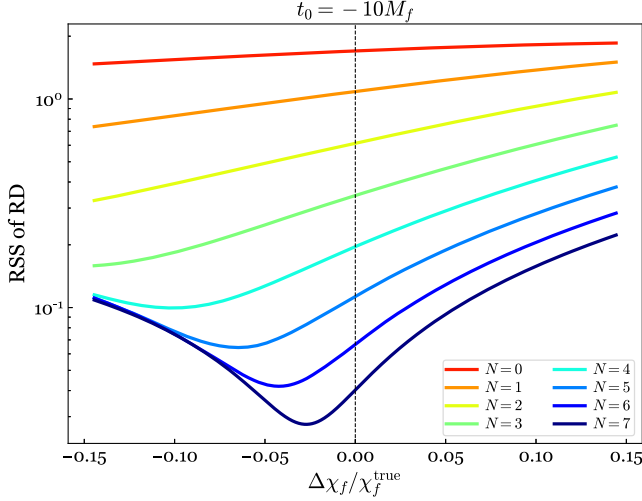
FIG. 15. Continuation of Fig. 14, except that the onset of the ringdown window t_0 is set to $-10M_f$.

panel of Fig. 14, we see that the ringdown RSS depends monotonically on χ_f when $t_0 = 0$ and $N = 0$, but the local minimum of the RSS does converge to the true value of χ_f after we include enough overtones. If we continue to go to an earlier regime, such as $t_0 = -10M_f$ in Fig. 15, we can see that the inferred spin is biased even when enough overtones are included, because of the presence of non-ringdown signals (e.g., late inspiral and merger). On the other hand, we also investigate the effect of M_f. We find that varying the value of M_f (with χ_f fixed to the true value) leads to a similar impact on the ringdown RSS, and the results are summarized in Appendix C.

Our results shown in Figs. 14 and 21 are closely related to Fig. 7 of Ref. [88], in which the authors show how the mismatch varies with deviations from GR and the start time of analyses. Similarly, our results indicate that the residual RSS depends strongly on the choice of (M_f, χ_f). In our case, a 2% change in χ_f can result in around two orders of magnitude change in the RSS, when t_0 and N are fixed to their "true" values.

After studying the effects of M_f and χ_f separately, in Fig. 16 we provide contours of RSS with varying them together. To avoid redundancy, we set t_0 to 0 and focus on two cases: $N = 2$ and $N = 7$, respectively. If we restrict ourselves to the region near the true remnant properties [Figs. 16(a) and 16(b)], the $N = 2$ one leads to biases in extracting M_f and χ_f, whereas the latter one can recover the remnant properties (marked with a cross) accurately. In addition, we notice that the effects of M_f and χ_f are partially degenerated—their difference $\sim M_f - \chi_f$ is more constrained than their sum $\sim M_f + \chi_f$. This is consistent with Figs. 10 and 11 of Ref. [101]. On the other hand, if we explore a larger parameter space (zoom out), we find there is a second local minimum in Fig. 16(c). To explore the

reason, in Fig. 17 we compare two filtered waveforms with χ_f and M_f chosen at their true values (red curve) and at the second local minimum (black curve), respectively. Recall that the amplitudes of adjacent overtones are out of phase, e.g., Refs. [101,176], they contribute destructively to the final ringdown waveform. Removing some overtones can increase the value of the filtered waveform at an early stage. On the contrary, when χ_f and M_f are at the second local minimum, even though the corresponding QNMs are not removed, the amplitude of the filtered waveform is reduced by around one order of magnitude. As a result, both cases lead to comparable RSS.

So far, we take (M_f, χ_f) as two independent variables. The QNM frequencies are obtained by assuming Kerr BHs with GR gravity. In Fig. 18, we relax this assumption and use the real and imaginary parts of a QNM as two independent variables. Here we restrict ourselves to the fundamental mode alone for simplicity, and take $t_0 = 50M_f$. We find the qualitative feature remains the same—there is a second local minimum, and the reason is exactly the same as that of Fig. 16(c).

Our discussions indicate that the filter could serve as a new tool to infer the remnant properties from actual detection data, and we refer the interested reader to our follow-up work [154] for more discussions.

VI. CONCLUSION

We have proposed two types of frequency-domain filters that are able to remove QNM(s) from ringdown signals. Our new method serves as a complementary tool to previous studies where the ringdown was analyzed in terms of time-domain fitting (e.g., Ref. [101]); it allows visualizing the existence of subdominant modes without the risk of overfitting. By applying our filter to the waveform of SXS:BBH:0305, we find the spherical-spheroidal mixing mode ω_{320} in harmonic h_{22}, the presence of ω_{220} in h_{21} due to the gravitational recoil, and second-order effects in h_{44}, h_{54} and h_{55} due to the quadratic coupling h_{22}^2 and $h_{22}h_{33}$. We also find the existence of retrograde modes in waveform SXS:BBH:1936. Our filter leads to an unphysical flipped ringdown prior to the start time of the real ringdown. Consequently, the late-inspiral and merger signals are contaminated.

Although the rational filter in Eq. (17) is constructed purely empirically, the full filter $\mathcal{F}_{lm}^D$ in Eq. (22) reflects the nature of the BH, and the filtered waveform corresponds to the image wave on the past horizon (Fig. 4). Furthermore, in spite of the unstable nature of QNM spectra [165,166], we find that the filter $\mathcal{F}_{lm}^D$ is stable in the time domain under the perturbations of the BH potential, in the sense that the original response remains unmodified, while the major correction appears as periodic echoes well separated from the original BH response. The time interval and amplitude of the echoes depend linearly on the parameters of the perturbation.
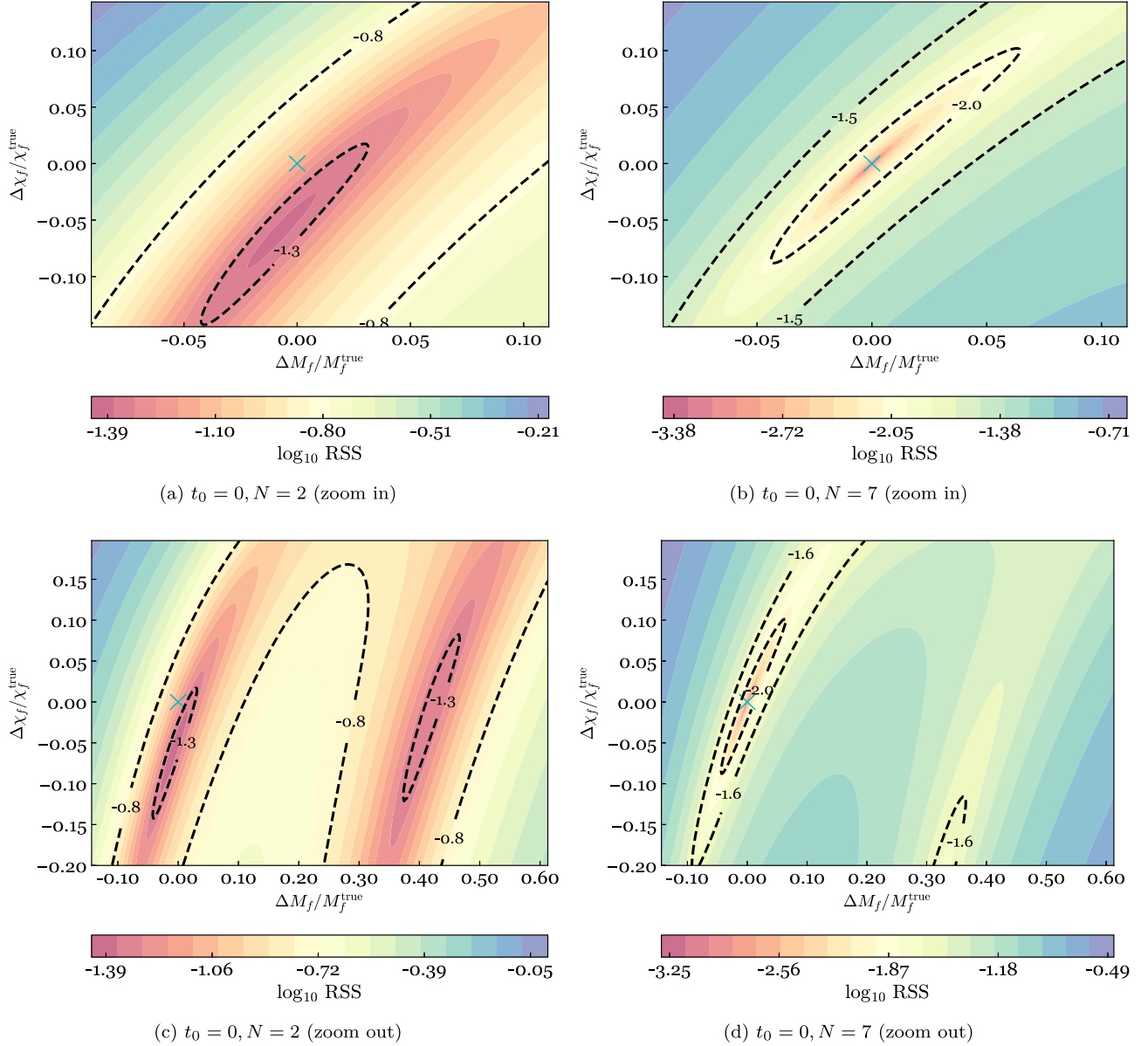
(a) $t_0 = 0, N = 2$ (zoom in)

(b) $t_0 = 0, N = 7$ (zoom in)

(c) $t_0 = 0, N = 2$ (zoom out)

(d) $t_0 = 0, N = 7$ (zoom out)

FIG. 16.   Contours of RSS with varying M_f and χ_f. To avoid redundancy, we set t_0 to 0 and choose $N = 2$ (left panels) and $N = 7$ (right panels). In the top row we explore the parameter space near the true remnant properties, whereas in the bottom row we investigate a larger area. The true remnant mass and spin are marked with a cross. The effects of M_f and χ_f are degenerate; their difference is more constrained than their sum. In addition, we find there is a second local minimum in Fig. 16(c).

Additionally, the rational filter takes the mass and spin of the remnant BH as free parameters. The residual ringdown RSS depends strongly on the choice of these two parameters. The true remnant properties could be recovered accurately from the ringdown of h_{22} as long as one consider a proper number of overtones and the start time of the analysis.

In this paper, we demonstrate that this new approach is powerful in ringdown analyses and outline a few applications. Future studies could be focused on:

(i) Nonlinearity due to the quadratic couplings. We focused exclusively on a few harmonics of SXS:

BBH:0305, and exhibited the existence of second-order effects only qualitatively. A more systematic study [158] is needed to investigate quadratic couplings in other BBH systems. We also refer the interested reader to Ref. [159] for relevant discussions.

(ii) Second-order effects in the multipole moments of dynamical horizons. Although Refs. [110,111] have shown that the multipole moments might be consistent with the superposition of linear QNMs soon after the formation of the common horizon, it is expected that a majority of nonlinearities are
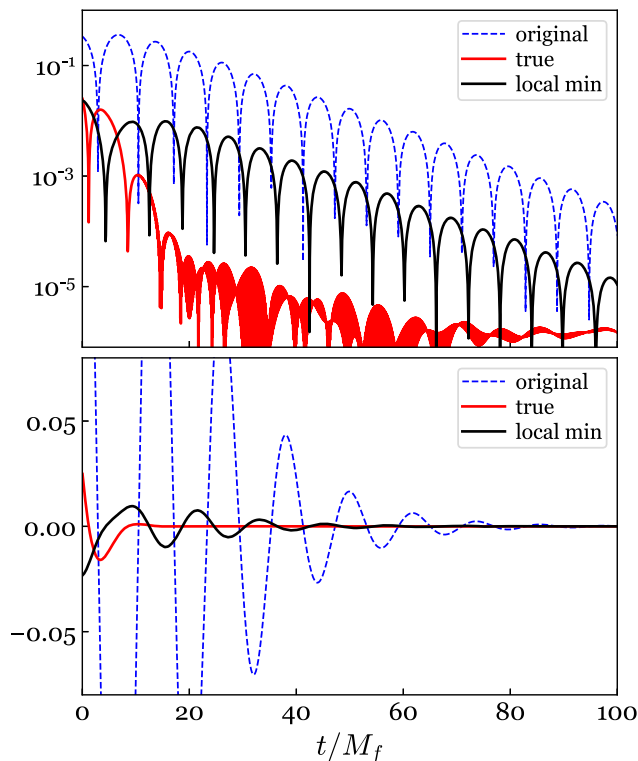
FIG. 17. An explanation for the second local minimum in Fig. 16(c). The blue dashed line corresponds to the original harmonic h_{22} of SXS:BBH:0305. Using the true remnant properties, the corresponding QNMs are removed (red curve). However, it has a larger amplitude at around 0. This is because adjacent overtones contribute destructively to the original waveform. Fewer QNMs reduce this cancellation and lead to a larger amplitude. On the contrary, using the remnant properties at the second local minimum (black curve), the amplitude of the original waveform diminishes even though the corresponding QNMs are not filtered away. As a result, two systems lead to similar RSS.

(a) $t_0 = 50M_f, N = 0$

FIG. 18. Same as Fig. 16, except that the real and imaginary parts of the fundamental mode are used as two independent variables. The start time t_0 is set to $50M_f$. Similar to Fig. 16(c), there is a second local minimum.

swallowed by horizons [89], which in turn should leave imprints on dynamical horizons. It is interesting to study these cases by applying our filters.

(iii) The stability of the two filters. In this work, we considered the stability of the full filter under a simple scenario: the perturbation arising only through a reflective boundary condition at the ECO surface that is very close to the would-be horizon. More sophisticated perturbations, e.g., the ones in Ref. [165,166], could be investigated. In addition, it might also be interesting to study the (in) stability of the rational filter. This requires high-precision calculations of QNMs of the new system. The goal of this trend is to answer how to distinguish a BH from its mimicker via our filters and how do the filters reflect the nature of the system?

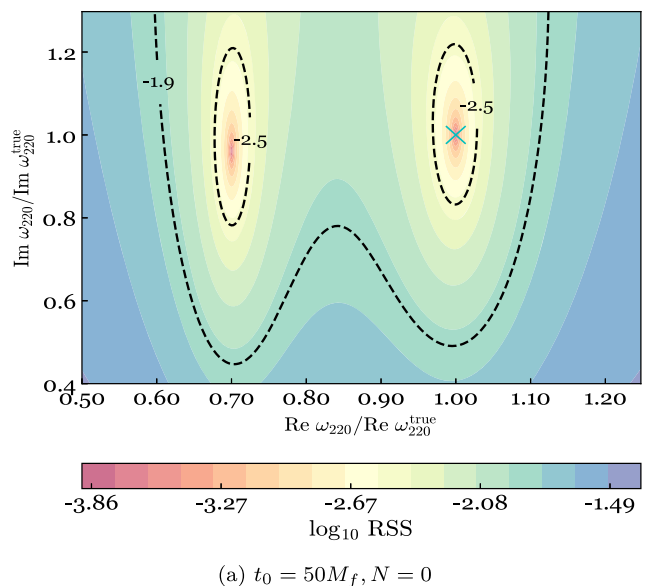(iv) Inferring remnant properties from real observational data. Here we restricted ourselves to a particular harmonic h_{22} and found that the remnant properties could be recovered accurately. A possible avenue for future work is to investigate the impact of our filters on the strain that is emitted toward a single angular direction. More importantly, one could apply our filter to real BBH events [154] and see whether we could place a tighter constraint on the remnant mass, spin, and also the no-hair theorem [52].

(v) Other filters. In this work, we have studied two related filters. One undesired feature of the rational filter is that it leads to a backward time shift, which makes it difficult to define the start time of the ringdown in the filtered waveform.[8] The full filter does not have this problem but is more computationally expensive to obtain. Therefore, it might be interesting to look for other new filters with better properties.

ACKNOWLEDGMENTS

---

[8]We show that the choice of the start time has a large impact on inferring remnant properties.

APPENDIX A: THE UP-MODE SOLUTION OF AN ECO

Near the ECO surface, Chen *et al.* [177] proposed a physical boundary condition via a family of zero-angular-momentum fiducial observers (FIDOs). The tidal tensor field within the rest frame of the FIDOs is given by [180]

$$\mathcal{E}_{ij} = h_i^a h_j^c C_{abcd} U^b U^d, \tag{A1a}$$

where C_{abcd} is the Weyl tensor, U^b is the four-velocity of the FIDOs, and $h_i^a = \delta_i^a + U^a U_i$ is the projection operator. Chen *et al.* argues that the tidal response of the ECO,

namely the reflection of incident GWs, is proportional to the transverse component of the tidal field,

$$\mathcal{E}_{\text{transverse}} \sim -\frac{\Delta}{4r^2}\psi_0 - \frac{r^2}{\Delta}\psi_4^*, \tag{A1b}$$

where ψ_0 and ψ_4 are the Weyl scalars. The coefficient depends on the nature of the ECO, such as the reflectivity $\mathcal{R}$ in Eq. (24). By adopting this type of boundary condition, Xin *et al.* [181] shows that the ratio between the reflective wave and the incident wave reads[9] [Eq. (56) of [181]],

$$\frac{\text{Reflective wave}}{\text{Incident wave}} = \frac{(-1)^{l+m+1}}{4}\mathcal{R}\frac{D_{lm}}{C_{lm}}, \tag{A1c}$$

with

$$D_{lm} = 64(2r_+)^4 ik(k^2 + 4\epsilon^2)\left(-ik + \frac{\sqrt{1-\chi^2}}{r_+}\right), \tag{A1d}$$

$$|C_{lm}|^2 = (Q^2 + 4\chi\omega m - 4\chi^2\omega^2)[(Q-2)^2 + 36\chi\omega m - 36\chi^2\omega^2] + 144\omega^2(1-\chi^2)$$
$$+ (2Q-1)(96\chi^2\omega^2 - 48\chi\omega m), \tag{A1e}$$

$$\text{Im}C_{lm} = 12\omega, \tag{A1f}$$

$$Q = \lambda + s(s+1) = \lambda + 2, \tag{A1g}$$

$$\epsilon = \frac{\sqrt{1-\chi^2}}{4r_+}, \tag{A1h}$$

$$k = \omega - m\Omega_+, \tag{A1i}$$

where λ is the eigenvalue of spin-weighted spheroidal harmonics and $\Omega_+ = \chi/(2r_+)$ is the horizon frequency.

As shown in Fig. 11, if we consider a GW emerging from the horizon with a unity amplitude (ignoring any r_* dependent coefficient), it will bounce back and forth within the cavity formed by the ECO surface and the BH potential. In particular, the observer at infinity will see a main transmissive wave with amplitude $1/D_{lm}^{\text{out}}$, followed by a series of echoes. Using the boundary condition in Eq. (A1c), it is straightforward to obtain the amplitude of the nth echo,

$$\frac{1}{D_{lm}^{\text{out}}}\left[\frac{(-1)^{l+m+1}}{4}\mathcal{R}\frac{D_{lm}}{C_{lm}}\frac{D_{lm}^{\text{in}}}{D_{lm}^{\text{out}}}\right]^n. \tag{A2}$$

By summing them together, we obtain the total transmissive amplitude,

$$\sum_n \frac{1}{D_{lm}^{\text{out}}}\left[\frac{(-1)^{l+m+1}}{4}\mathcal{R}\frac{D_{lm}}{C_{lm}}\frac{D_{lm}^{\text{in}}}{D_{lm}^{\text{out}}}\right]^n$$
$$= \frac{1}{D_{lm}^{\text{out}}}\frac{1}{1 - \frac{(-1)^{l+m+1}}{4}\mathcal{R}\frac{D_{lm}}{C_{lm}}\frac{D_{lm}^{\text{in}}}{D_{lm}^{\text{out}}}}. \tag{A3}$$

The inverse of the total amplitude corresponds to $\tilde{D}_{lm}^{\text{out}}$ in Eq. (25).

APPENDIX B: $\mathcal{F}_{22}^{DECO}$ FOR A SPINNING ECO

Figures 19 and 20 show the filter $\mathcal{F}_{22}^{DECO}$ in the time and frequency domain. The spin of the ECO is $\chi_f = 0.692$. It has the same qualitative features as that of the nonspinning ECO (Fig. 12).
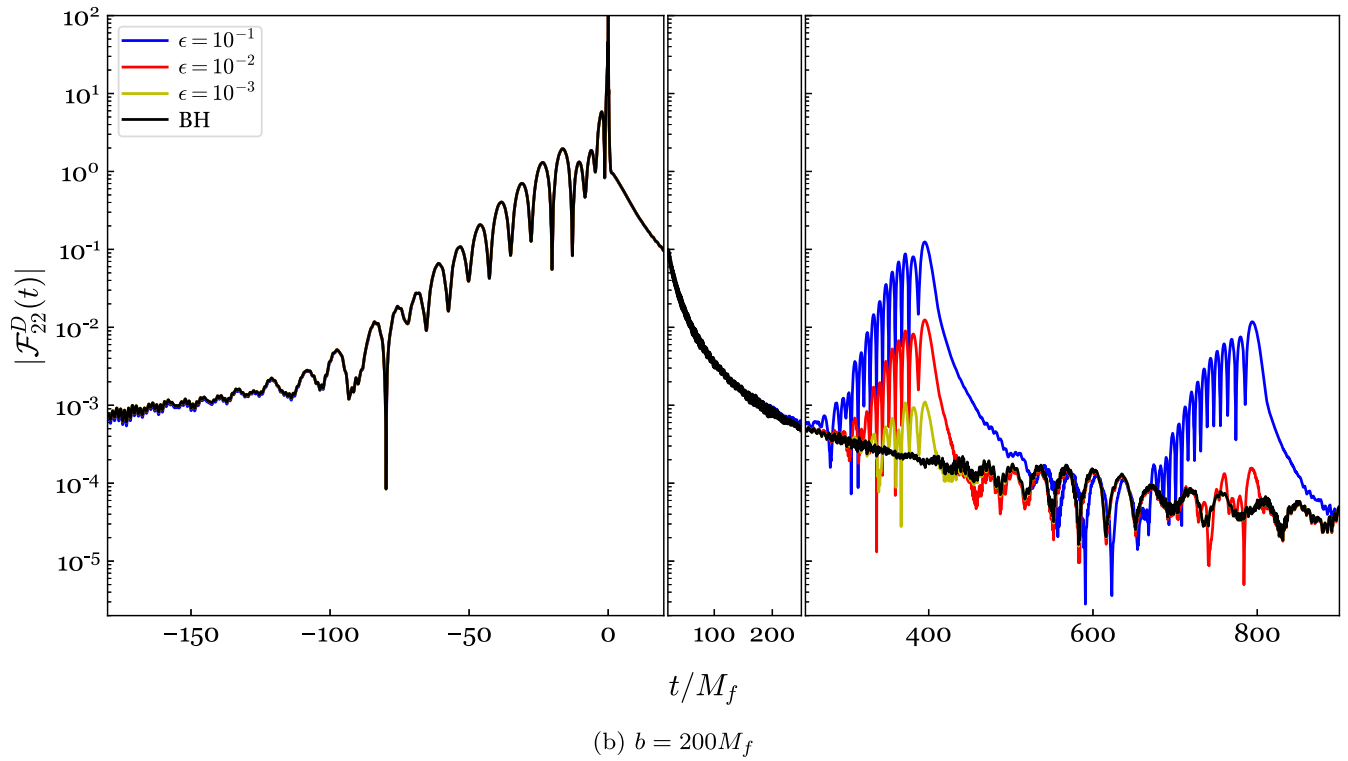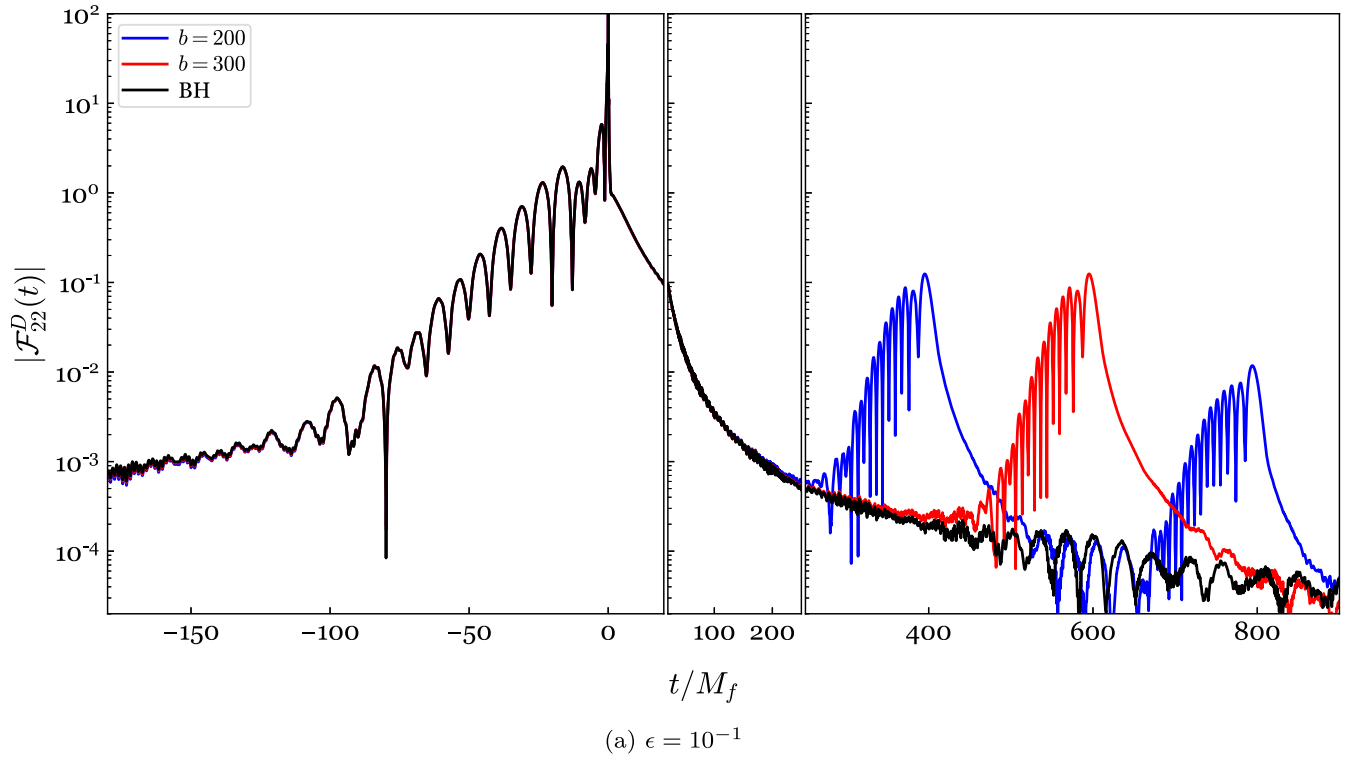
---

[9]The additional factor $(-1)^l$ is due to the assumption that the system is invariant under reflection across the $x - y$ plane [182].

(a) $\epsilon = 10^{-1}$

(b) $b = 200 M_f$

FIG. 19. Same as Fig. 12, but for a spinning ECO with $\chi_f = 0.692$.

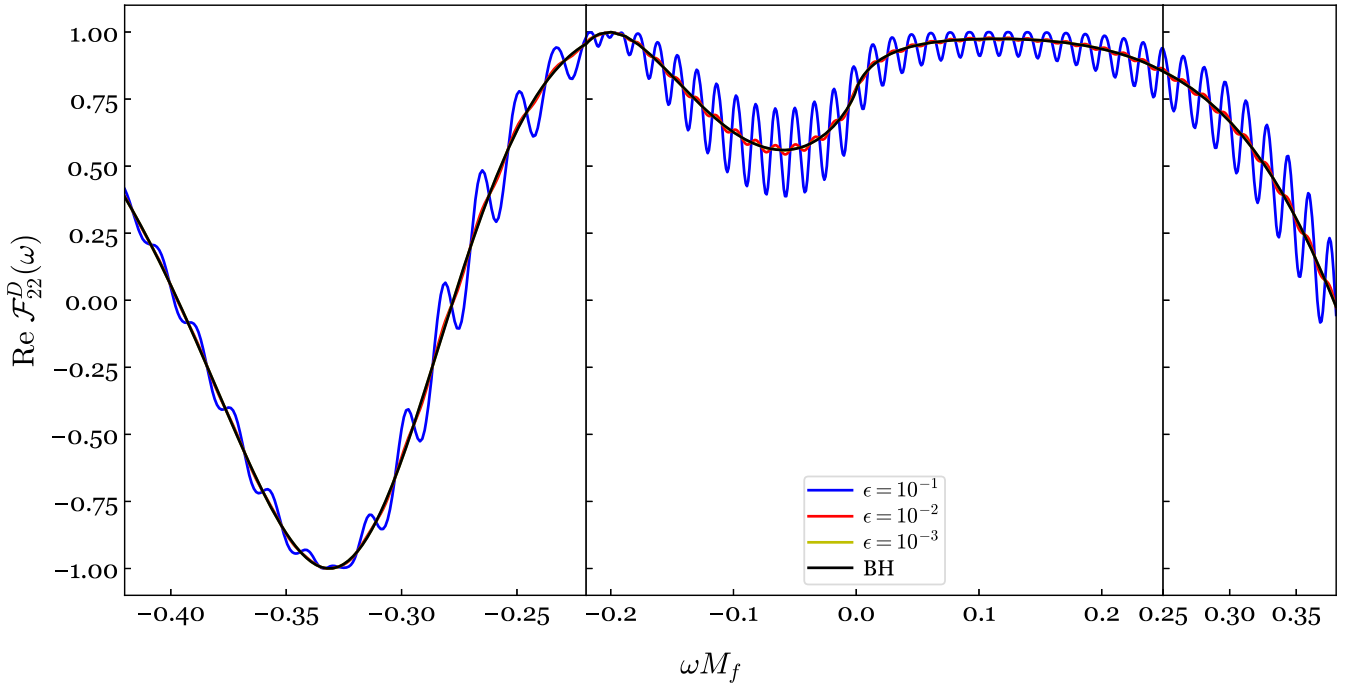(a) $\epsilon = 10^{-1}$
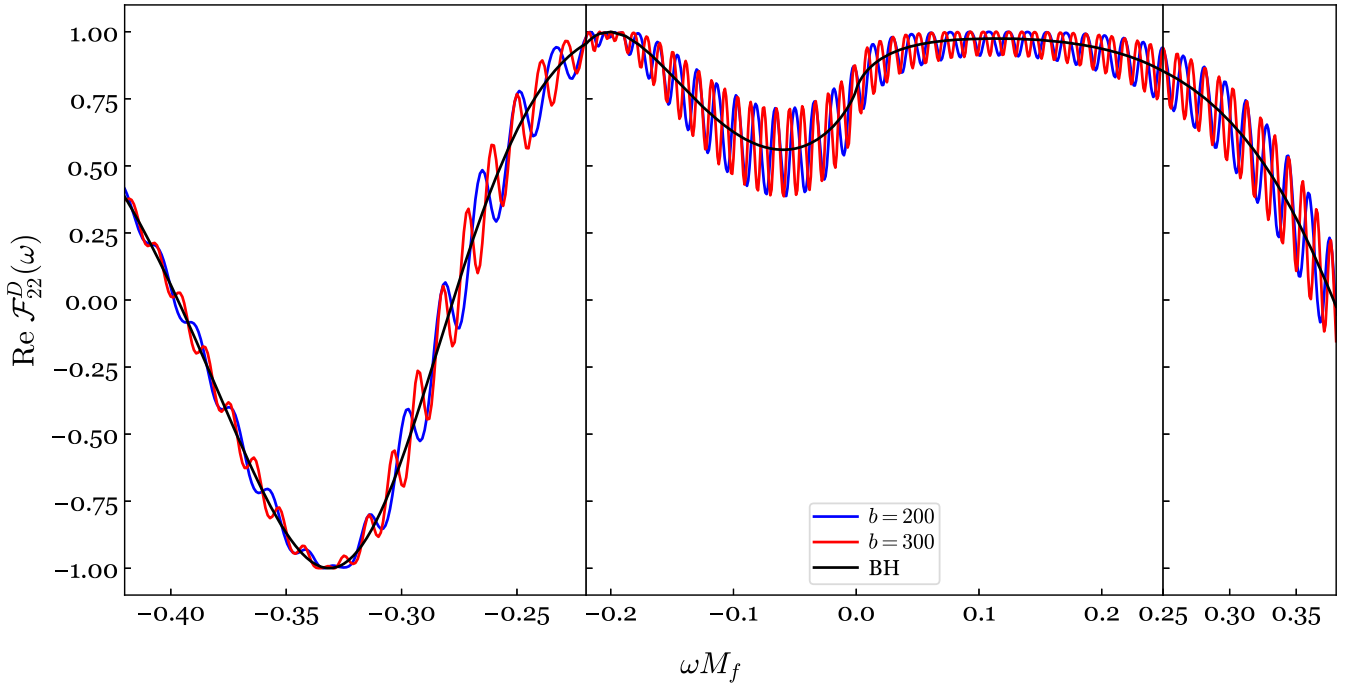

(b) $b = 200 M_f$

FIG. 20.   Same as Fig. 13, but for a spinning ECO with $\chi_f = 0.692$.

APPENDIX C: M_f AND RSS

In Fig. 21, we plot the ringdown RSS of the filtered waveform as a function of the remnant mass M_f, using waveform SXS:BBH:0305.
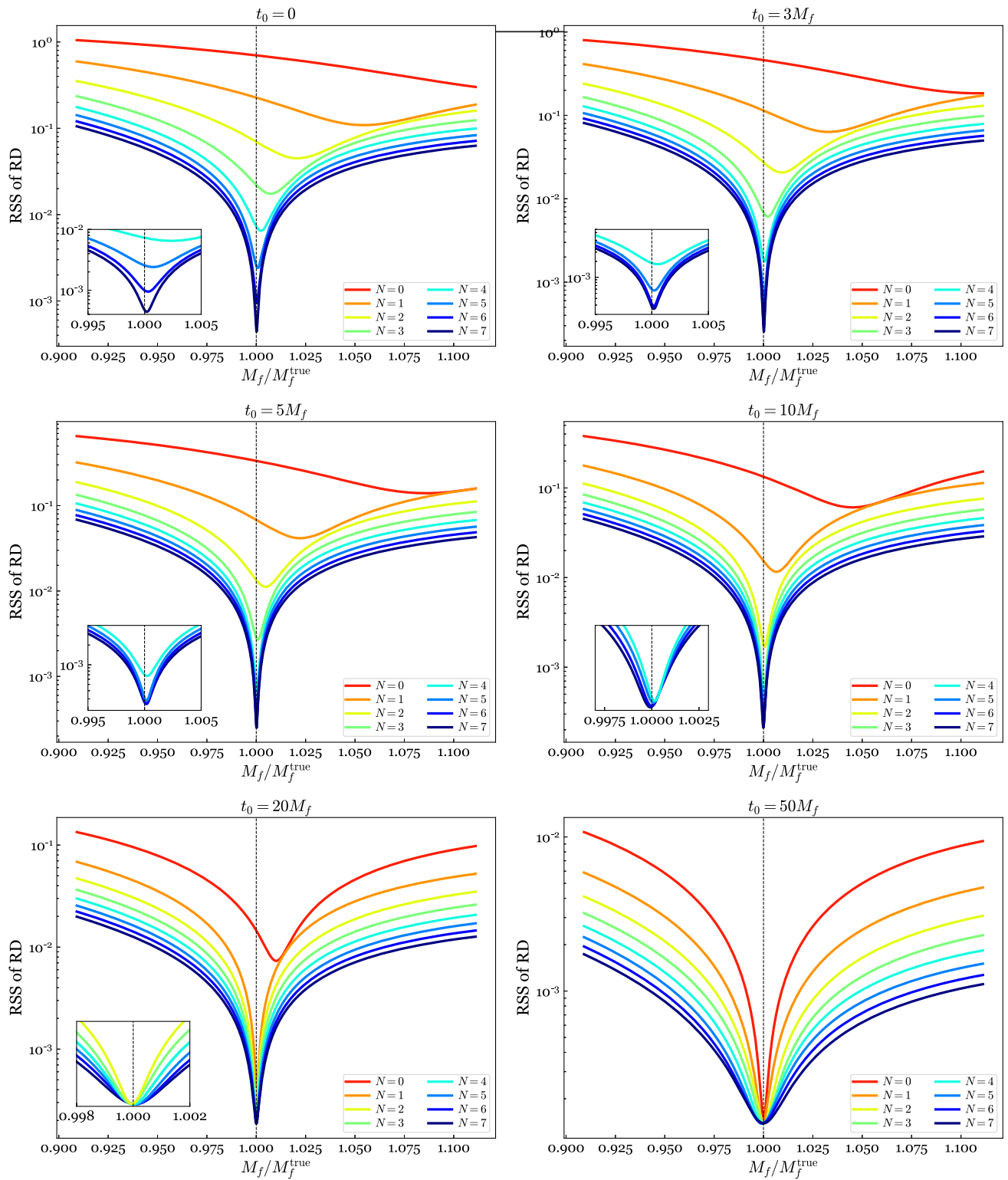

FIG. 21. Same as Fig. 14, but with varying M_f and fixed χ_f.

[1] B. P. Abbott *et al.* (LIGO Scientific, Virgo Collaborations), Binary Black Hole Mergers in the first Advanced LIGO Observing Run, Phys. Rev. X **6,** 041015 (2016); **8,** 039903 (E) (2018).

[2] B. P. Abbott *et al.* (LIGO Scientific, Virgo Collaborations), GWTC-1: A Gravitational-Wave Transient Catalog of Compact Binary Mergers Observed by LIGO and Virgo during the First and Second Observing Runs, Phys. Rev. X **9,** 031040 (2019).

[3] R. Abbott *et al.* (LIGO Scientific, Virgo Collaborations), GWTC-2: Compact Binary Coalescences Observed by LIGO and Virgo During the First Half of the Third Observing Run, Phys. Rev. X **11,** 021053 (2021).

[4] R. Abbott *et al.* (LIGO Scientific, VIRGO, KAGRA Collaborations), GWTC-3: Compact binary coalescences observed by LIGO and Virgo during the second part of the third observing run, arXiv:2111.03606.

[5] J. Aasi *et al.* (LSC Collaboration), Advanced LIGO, Classical Quantum Gravity **32,** 115012 (2015).

[6] F. Acernese *et al.* (Virgo Collaboration), Advanced Virgo: A second-generation interferometric gravitational wave detector, Classical Quantum Gravity **32,** 024001 (2015).

[7] Y. Aso, Y. Michimura, K. Somiya, M. Ando, O. Miyakawa, T. Sekiguchi, D. Tatsumi, and H. Yamamoto (The KAGRA Collaboration), Interferometer design of the KAGRA gravitational wave detector, Phys. Rev. D **88,** 043007 (2013).

[8] K. D. Kokkotas and B. G. Schmidt, Quasinormal modes of stars and black holes, Living Rev. Relativity **2,** 2 (1999).

[9] H.-P. Nollert, Quasinormal modes: The characteristic 'sound' of black holes and neutron stars, Classical Quantum Gravity **16,** R159 (1999).

[10] V. Cardoso and L. Gualtieri, Testing the black hole 'no-hair' hypothesis, Classical Quantum Gravity **33,** 174001 (2016).

[11] E. Berti, V. Cardoso, and A. O. Starinets, Quasinormal modes of black holes and black branes, Classical Quantum Gravity **26,** 163001 (2009).

[12] R. H. Price, Nonspherical perturbations of relativistic gravitational collapse. I. Scalar and gravitational perturbations, Phys. Rev. D **5,** 2419 (1972).

[13] R. H. Price, Nonspherical perturbations of relativistic gravitational collapse. II. Integer-spin, zero-rest-mass fields, Phys. Rev. D **5,** 2439 (1972).

[14] R. Penrose, "golden oldie": Gravitational collapse: The role of general relativity, Gen. Relativ. Gravit. **34,** 1141 (2002).

[15] P. T. Chrusciel, J. Lopes Costa, and M. Heusler, Stationary black holes: Uniqueness and beyond, Living Rev. Relativity **15,** 7 (2012).

[16] B. Carter, Axisymmetric Black Hole Has Only Two Degrees of Freedom, Phys. Rev. Lett. **26,** 331 (1971).

[17] W. Israel, Event horizons in static vacuum space-times, Phys. Rev. **164,** 1776 (1967).

[18] F. Echeverria, Gravitational-wave measurements of the mass and angular momentum of a black hole, Phys. Rev. D **40,** 3194 (1989).

[19] O. Dreyer, B. J. Kelly, B. Krishnan, L. S. Finn, D. Garrison, and R. Lopez-Aleman, Black hole spectroscopy: Testing general relativity through gravitational wave observations, Classical Quantum Gravity **21,** 787 (2004).

[20] E. Berti, V. Cardoso, and C. M. Will, On gravitational-wave spectroscopy of massive black holes with the space interferometer LISA, Phys. Rev. D **73,** 064030 (2006).

[21] E. Berti, J. Cardoso, V. Cardoso, and M. Cavaglia, Matched-filtering and parameter estimation of ringdown waveforms, Phys. Rev. D **76,** 104044 (2007).

[22] S. Gossan, J. Veitch, and B. S. Sathyaprakash, Bayesian model selection for testing the no-hair theorem with black hole ringdowns, Phys. Rev. D **85,** 124056 (2012).

[23] S. Caudill, S. E. Field, C. R. Galley, F. Herrmann, and M. Tiglio, Reduced Basis representations of multi-mode black hole ringdown gravitational waves, Classical Quantum Gravity **29,** 095016 (2012).

[24] J. Meidam, M. Agathos, C. Van Den Broeck, J. Veitch, and B. S. Sathyaprakash, Testing the no-hair theorem with black hole ringdowns using TIGER, Phys. Rev. D **90,** 064009 (2014).

[25] S. Bhagwat, D. A. Brown, and S. W. Ballmer, Spectroscopic analysis of stellar mass black-hole mergers in our local universe with ground-based gravitational wave detectors, Phys. Rev. D **94,** 084024 (2016); **95,** 069906(E) (2017).

[26] E. Berti, A. Sesana, E. Barausse, V. Cardoso, and K. Belczynski, Spectroscopy of Kerr Black Holes with Earth- and Space-Based Interferometers, Phys. Rev. Lett. **117,** 101102 (2016).

[27] V. Baibhav, E. Berti, V. Cardoso, and G. Khanna, Black hole spectroscopy: Systematic errors and ringdown energy estimates, Phys. Rev. D **97,** 044048 (2018).

[28] A. Maselli, K. Kokkotas, and P. Laguna, Observing binary black hole ringdowns by advanced gravitational wave detectors, Phys. Rev. D **95,** 104026 (2017).

[29] H. Yang, K. Yagi, J. Blackman, L. Lehner, V. Paschalidis, F. Pretorius, and N. Yunes, Black Hole Spectroscopy with Coherent Mode Stacking, Phys. Rev. Lett. **118,** 161101 (2017).

[30] C. F. Da Silva Costa, S. Tiwari, S. Klimenko, and F. Salemi, Detection of (2,2) quasinormal mode from a population of black holes with a constructive summation method, Phys. Rev. D **98,** 024052 (2018).

[31] V. Baibhav and E. Berti, Multimode black hole spectroscopy, Phys. Rev. D **99,** 024005 (2019).

[32] G. Carullo *et al.*, Empirical tests of the black hole no-hair conjecture using gravitational-wave observations, Phys. Rev. D **98,** 104020 (2018).

[33] R. Brito, A. Buonanno, and V. Raymond, Black-hole spectroscopy by making full use of gravitational-wave modeling, Phys. Rev. D **98,** 084038 (2018).

[34] H. Nakano, T. Narikawa, K.-i. Oohara, K. Sakai, H.-a. Shinkai, H. Takahashi, T. Tanaka, N. Uchikata, S. Yamamoto, and T. S. Yamamoto, Comparison of various methods to extract ringdown frequency from gravitational wave data, Phys. Rev. D **99,** 124032 (2019).

[35] M. Cabero, J. Westerweck, C. D. Capano, S. Kumar, A. B. Nielsen, and B. Krishnan, Black hole spectroscopy in the next decade, Phys. Rev. D **101,** 064044 (2020).

[36] S. Bhagwat, M. Cabero, C. D. Capano, B. Krishnan, and D. A. Brown, Detectability of the subdominant mode in a

binary black hole ringdown, Phys. Rev. D **102,** 024023 (2020).

[37] I. Ota and C. Chirenti, Overtones or higher harmonics? Prospects for testing the no-hair theorem with gravitational wave detections, Phys. Rev. D **101,** 104005 (2020).

[38] J. C. Bustillo, P. D. Lasky, and E. Thrane, Black-hole spectroscopy, the no-hair theorem, and GW150914: Kerr versus Occam, Phys. Rev. D **103,** 024041 (2021).

[39] X. Jiménez Forteza, S. Bhagwat, P. Pani, and V. Ferrari, Spectroscopy of binary black hole ringdown using overtones and angular modes, Phys. Rev. D **102,** 044053 (2020).

[40] M. Isi and W. M. Farr, Analyzing black-hole ringdowns, arXiv:2107.05609.

[41] E. Finch and C. J. Moore, Frequency-domain analysis of black-hole ringdowns, Phys. Rev. D **104,** 123034 (2021).

[42] V. Cardoso and P. Pani, Tests for the existence of black holes through gravitational wave echoes, Nat. Astron. **1,** 586 (2017).

[43] V. Cardoso, E. Franzin, and P. Pani, Is the Gravitational-Wave Ringdown a Probe of the Event Horizon?, Phys. Rev. Lett. **116,** 171101 (2016); **117,** 089902(E) (2016).

[44] V. F. Foit and M. Kleban, Testing quantum black holes with gravitational waves, Classical Quantum Gravity **36,** 035006 (2019).

[45] D. Laghi, G. Carullo, J. Veitch, and W. Del Pozzo, Quantum black hole spectroscopy: Probing the quantum nature of the black hole area using LIGO–Virgo ringdown detections, Classical Quantum Gravity **38,** 095005 (2021).

[46] J. L. Blázquez-Salcedo, C. F. B. Macedo, V. Cardoso, V. Ferrari, L. Gualtieri, F. S. Khoo, J. Kunz, and P. Pani, Perturbed black holes in Einstein-dilaton-Gauss-Bonnet gravity: Stability, ringdown, and gravitational-wave emission, Phys. Rev. D **94,** 104024 (2016).

[47] K. Glampedakis, G. Pappas, H. O. Silva, and E. Berti, Post-Kerr black hole spectroscopy, Phys. Rev. D **96,** 064054 (2017).

[48] H. O. Silva, A. Ghosh, and A. Buonanno, Black-hole ringdown as a probe of higher-curvature gravity theories, arXiv:2205.05132.

[49] A. Maselli, P. Pani, L. Gualtieri, and E. Berti, Parametrized ringdown spin expansion coefficients: A data-analysis framework for black-hole spectroscopy with multiple events, Phys. Rev. D **101,** 024043 (2020).

[50] B. P. Abbott *et al.* (LIGO Scientific, Virgo Collaborations), Observation of Gravitational Waves from a Binary Black Hole Merger, Phys. Rev. Lett. **116,** 061102 (2016).

[51] G. Carullo, W. Del Pozzo, and J. Veitch, Observational black hole spectroscopy: A time-domain multimode analysis of GW150914, Phys. Rev. D **99,** 123029 (2019); **100,** 089903(E) (2019).

[52] M. Isi, M. Giesler, W. M. Farr, M. A. Scheel, and S. A. Teukolsky, Testing the No-Hair Theorem with GW150914, Phys. Rev. Lett. **123,** 111102 (2019).

[53] R. Cotesta, G. Carullo, E. Berti, and V. Cardoso, On the Detection of Ringdown Overtones in GW150914, Phys. Rev. Lett. **129,** 111102 (2022).

[54] M. Isi and W. M. Farr, Revisiting the ringdown of GW150914, arXiv:2202.02941.

[55] E. Finch and C. J. Moore, Searching for a ringdown overtone in GW150914, Phys. Rev. D **106,** 043005 (2022).

[56] C. D. Capano, M. Cabero, J. Westerweck, J. Abedi, S. Kastha, A. H. Nitz, A. B. Nielsen, and B. Krishnan, Observation of a multimode quasi-normal spectrum from a perturbed black hole, arXiv:2105.05238.

[57] R. Abbott *et al.* (LIGO Scientific, Virgo Collaborations), GW190521: A Binary Black Hole Merger with a Total Mass of 150 $M_\odot$, Phys. Rev. Lett. **125,** 101102 (2020).

[58] R. Abbott *et al.* (LIGO Scientific, Virgo Collaborations), Tests of general relativity with binary black holes from the second LIGO-Virgo gravitational-wave transient catalog, Phys. Rev. D **103,** 122002 (2021).

[59] R. Abbott *et al.* (LIGO Scientific, VIRGO, KAGRA Collaborations), Tests of general relativity with GWTC-3, arXiv:2112.06861.

[60] A. Ghosh, R. Brito, and A. Buonanno, Constraints on quasinormal-mode frequencies with LIGO-Virgo binary–black-hole observations, Phys. Rev. D **103,** 124041 (2021).

[61] S. A. Hughes and K. Menou, Golden binaries for LISA: Robust probes of strong-field gravity, Astrophys. J. **623,** 689 (2005).

[62] M. Luna and A. M. Sintes, Parameter estimation of compact binaries using the inspiral and ringdown waveforms, Classical Quantum Gravity **23,** 3763 (2006).

[63] H. Nakano, T. Tanaka, and T. Nakamura, Possible golden events for ringdown gravitational waves, Phys. Rev. D **92,** 064003 (2015).

[64] A. Ghosh, N. K. Johnson-Mcdaniel, A. Ghosh, C. K. Mishra, P. Ajith, W. Del Pozzo, C. P. L. Berry, A. B. Nielsen, and L. London, Testing general relativity using gravitational wave signals from the inspiral, merger and ringdown of binary black holes, Classical Quantum Gravity **35,** 014002 (2018).

[65] A. Ghosh *et al.*, Testing general relativity using golden black-hole binaries, Phys. Rev. D **94,** 021101 (2016).

[66] B. P. Abbott *et al.* (LIGO Scientific, Virgo Collaborations), Tests of General Relativity with GW150914, Phys. Rev. Lett. **116,** 221101 (2016); **121,** 129902(E) (2018).

[67] B. P. Abbott *et al.* (LIGO Scientific, VIRGO Collaborations), GW170104: Observation of a 50-Solar-Mass Binary Black Hole Coalescence at Redshift 0.2, Phys. Rev. Lett. **118,** 221101 (2017); **121,** 129901(E) (2018).

[68] B. P. Abbott *et al.* (LIGO Scientific, Virgo Collaborations), Tests of General Relativity with the Binary Black Hole Signals from the LIGO-Virgo Catalog GWTC-1, Phys. Rev. D **100,** 104036 (2019).

[69] M. Breschi, R. O'Shaughnessy, J. Lange, and O. Birnholtz, IMR consistency tests with higher modes on gravitational signals from the second observing run of LIGO and Virgo, Classical Quantum Gravity **36,** 245019 (2019).

[70] M. Cabero, C. D. Capano, O. Fischer-Birnholtz, B. Krishnan, A. B. Nielsen, A. H. Nitz, and C. M. Biwer, Observational tests of the black hole area increase law, Phys. Rev. D **97,** 124069 (2018).

[71] M. Isi, W. M. Farr, M. Giesler, M. A. Scheel, and S. A. Teukolsky, Testing the Black-Hole Area Law with GW150914, Phys. Rev. Lett. **127,** 011103 (2021).

[72] S. W. Hawking, Gravitational Radiation from Colliding Black Holes, Phys. Rev. Lett. **26,** 1344 (1971).

[73] Y. Sun and R. H. Price, Excitation of quasinormal ringing of a schwarzschild black hole, Phys. Rev. D **38,** 1040 (1988).

[74] Y. Sun and R. H. Price, Excitation of schwarzschild quasinormal modes by collapse, Phys. Rev. D **41,** 2492 (1990).

[75] E. N. Dorband, E. Berti, P. Diener, E. Schnetter, and M. Tiglio, A Numerical study of the quasinormal mode excitation of Kerr black holes, Phys. Rev. D **74,** 084028 (2006).

[76] E. Berti and V. Cardoso, Quasinormal ringing of Kerr black holes. I. The excitation factors, Phys. Rev. D **74,** 104020 (2006).

[77] S. Hadar, B. Kol, E. Berti, and V. Cardoso, Comparing numerical and analytical calculations of post-ISCO ring-down amplitudes, Phys. Rev. D **84,** 047501 (2011).

[78] S. Hadar and B. Kol, Post-ISCO ringdown amplitudes in extreme mass ratio inspiral, Phys. Rev. D **84,** 044019 (2011).

[79] I. Kamaretsos, M. Hannam, S. Husa, and B. S. Sathyaprakash, Black-hole hair loss: Learning about binary progenitors from ringdown signals, Phys. Rev. D **85,** 024018 (2012).

[80] Z. Zhang, E. Berti, and V. Cardoso, Quasinormal ringing of Kerr black holes. II. Excitation by particles falling radially with arbitrary energy, Phys. Rev. D **88,** 044018 (2013).

[81] L. T. London, Modeling ringdown. II. Aligned-spin binary black holes, implications for data analysis and fundamental theory, Phys. Rev. D **102,** 084052 (2020).

[82] S. A. Hughes, A. Apte, G. Khanna, and H. Lim, Learning about Black Hole Binaries from their Ringdown Spectra, Phys. Rev. Lett. **123,** 161101 (2019).

[83] A. Apte and S. A. Hughes, Exciting black hole modes via misaligned coalescences: I. Inspiral, transition, and plunge trajectories using a generalized Ori-Thorne procedure, Phys. Rev. D **100,** 084031 (2019).

[84] H. Lim, G. Khanna, and S. A. Hughes, Measuring quasi-normal mode amplitudes with misaligned binary black hole ringdowns, Phys. Rev. D **105,** 124030 (2022).

[85] H. Lim, G. Khanna, A. Apte, and S. A. Hughes, Exciting black hole modes via misaligned coalescences: II. The mode content of late-time coalescence waveforms, Phys. Rev. D **100,** 084032 (2019).

[86] P. A. Cano, K. Fransen, T. Hertog, and S. Maenaut, Gravitational ringing of rotating black holes in higher-derivative gravity, Phys. Rev. D **105,** 024064 (2022).

[87] S. Bhagwat, M. Okounkova, S. W. Ballmer, D. A. Brown, M. Giesler, M. A. Scheel, and S. A. Teukolsky, On choosing the start time of binary black hole ringdowns, Phys. Rev. D **97,** 104065 (2018).

[88] S. Bhagwat, X. J. Forteza, P. Pani, and V. Ferrari, Ring-down overtones, black hole spectroscopy, and no-hair theorem tests, Phys. Rev. D **101,** 044033 (2020).

[89] M. Okounkova, Revisiting non-linearity in binary black hole mergers, arXiv:2004.00671.

[90] F. Pretorius, Evolution of Binary Black Hole Spacetimes, Phys. Rev. Lett. **95,** 121101 (2005).

[91] A. Buonanno, G. B. Cook, and F. Pretorius, Inspiral, merger and ring-down of equal-mass black-hole binaries, Phys. Rev. D **75,** 124018 (2007).

[92] E. Berti, V. Cardoso, J. A. Gonzalez, U. Sperhake, M. Hannam, S. Husa, and B. Bruegmann, Inspiral, merger and ringdown of unequal mass black hole binaries: A multi-polar analysis, Phys. Rev. D **76,** 064034 (2007).

[93] E. Berti, V. Cardoso, J. A. Gonzalez, and U. Sperhake, Mining information from binary black hole mergers: A comparison of estimation methods for complex exponentials in noise, Phys. Rev. D **75,** 124017 (2007).

[94] L. London, D. Shoemaker, and J. Healy, Modeling ring-down: Beyond the fundamental quasinormal modes, Phys. Rev. D **90,** 124032 (2014); **94,** 069902(E) (2016).

[95] A. Taracchini, Y. Pan, A. Buonanno, E. Barausse, M. Boyle, T. Chu, G. Lovelace, H. P. Pfeiffer, and M. A. Scheel, Prototype effective-one-body model for nonpre-cessing spinning inspiral-merger-ringdown waveforms, Phys. Rev. D **86,** 024011 (2012).

[96] Y. Pan, A. Buonanno, M. Boyle, L. T. Buchman, L. E. Kidder, H. P. Pfeiffer, and M. A. Scheel, Inspiral-merger-ringdown multipolar waveforms of nonspinning black-hole binaries using the effective-one-body formalism, Phys. Rev. D **84,** 124052 (2011).

[97] A. Taracchini *et al.*, Effective-one-body model for black-hole binaries with generic mass ratios and spins, Phys. Rev. D **89,** 061502 (2014).

[98] T. Damour and A. Nagar, A new analytic representation of the ringdown waveform of coalescing spinning black hole binaries, Phys. Rev. D **90,** 024054 (2014).

[99] A. Taracchini, A. Buonanno, G. Khanna, and S. A. Hughes, Small mass plunging into a Kerr black hole: Anatomy of the inspiral-merger-ringdown waveforms, Phys. Rev. D **90,** 084025 (2014).

[100] E. Thrane, P. D. Lasky, and Y. Levin, Challenges testing the no-hair theorem with gravitational waves, Phys. Rev. D **96,** 102004 (2017).

[101] M. Giesler, M. Isi, M. A. Scheel, and S. Teukolsky, Black Hole Ringdown: The Importance of Overtones, Phys. Rev. X **9,** 041060 (2019).

[102] G. B. Cook, Aspects of multimode Kerr ringdown fitting, Phys. Rev. D **102,** 024027 (2020).

[103] A. Dhani, Importance of mirror modes in binary black hole ringdown waveform, Phys. Rev. D **103,** 104048 (2021).

[104] X. J. Forteza and P. Mourier, High-overtone fits to numeri-cal relativity ringdowns: Beyond the dismissed $n = 8$ special tone, Phys. Rev. D **104,** 124072 (2021).

[105] E. Finch and C. J. Moore, Modeling the ringdown from precessing black hole binaries, Phys. Rev. D **103,** 084048 (2021).

[106] X. Li, L. Sun, R. K. L. Lo, E. Payne, and Y. Chen, Angular emission patterns of remnant black holes, Phys. Rev. D **105,** 024016 (2022).

[107] L. Magaña Zertuche *et al.*, High precision ringdown modeling: Multimode fits and BMS frames, Phys. Rev. D **105,** 104015 (2022).

[108] K. Mitman, J. Moxon, M. A. Scheel, S. A. Teukolsky, M. Boyle, N. Deppe, L. E. Kidder, and W. Throwe, Compu-tation of displacement and spin gravitational memory in numerical relativity, Phys. Rev. D **102,** 104007 (2020).

[109] K. Mitman *et al.*, Adding gravitational memory to waveform catalogs using BMS balance laws, Phys. Rev. D **103**, 024031 (2021).

[110] D. Pook-Kolb, O. Birnholtz, J. L. Jaramillo, B. Krishnan, and E. Schnetter, Horizons in a binary black hole merger II: Fluxes, multipole moments and stability, arXiv:2006.03940.

[111] P. Mourier, X. Jiménez Forteza, D. Pook-Kolb, B. Krishnan, and E. Schnetter, Quasinormal modes and their overtones at the common horizon in a binary black hole merger, Phys. Rev. D **103**, 044054 (2021).

[112] R. J. Gleiser, C. O. Nicasio, R. H. Price, and J. Pullin, Colliding Black Holes: How Far Can the Close Approximation Go?, Phys. Rev. Lett. **77**, 4483 (1996).

[113] K. Tomita and N. Tajima, Nonlinear behavior of nonspherical perturbations of the schwarzschild metric, Prog. Theor. Phys. **56**, 551 (1976).

[114] K. Tomita, On the non-linear behavior of nonspherical perturbations in relativistic gravitational collapse, Prog. Theor. Phys. **52**, 1188 (1974).

[115] C. T. Cunningham, R. H. Price, and V. Moncrief, Radiation from collapsing relativistic stars. III—Second order perturbations of collapse with rotation, Astrophys. J. **236**, 674 (1980).

[116] R. H. Price and J. Pullin, Colliding Black Holes: The Close Limit, Phys. Rev. Lett. **72**, 3297 (1994).

[117] R. J. Gleiser, C. O. Nicasio, R. H. Price, and J. Pullin, Second order perturbations of a Schwarzschild black hole, Classical Quantum Gravity **13**, L117 (1996).

[118] R. J. Gleiser, C. O. Nicasio, R. H. Price, and J. Pullin, Gravitational radiation from Schwarzschild black holes: The second order perturbation formalism, Phys. Rep. **325**, 41 (2000).

[119] C. O. Nicasio, R. Gleiser, and J. Pullin, Second order perturbations of a Schwarzschild black hole: Inclusion of odd parity perturbations, Gen. Relativ. Gravit. **32**, 2021 (2000).

[120] D. Brizuela, J. M. Martin-Garcia, and G. A. Mena Marugan, Second and higher-order perturbations of a spherical spacetime, Phys. Rev. D **74**, 044039 (2006).

[121] D. Brizuela, J. M. Martin-Garcia, and G. A. M. Marugan, High-order gauge-invariant perturbations of a spherical spacetime, Phys. Rev. D **76**, 024004 (2007).

[122] D. Brizuela, J. M. Martin-Garcia, and M. Tiglio, A complete gauge-invariant formalism for arbitrary second-order perturbations of a Schwarzschild black hole, Phys. Rev. D **80**, 024021 (2009).

[123] M. Campanelli and C. O. Lousto, Second order gauge invariant gravitational perturbations of a Kerr black hole, Phys. Rev. D **59**, 124022 (1999).

[124] S. R. Green, S. Hollands, and P. Zimmerman, Teukolsky formalism for nonlinear Kerr perturbations, Classical Quantum Gravity **37**, 075001 (2020).

[125] N. Loutrel, J. L. Ripley, E. Giorgi, and F. Pretorius, Second order perturbations of Kerr black holes: Reconstruction of the metric, Phys. Rev. D **103**, 104017 (2021).

[126] J. L. Ripley, N. Loutrel, E. Giorgi, and F. Pretorius, Numerical computation of second order vacuum perturbations of Kerr black holes, Phys. Rev. D **103**, 104018 (2021).

[127] Y. Zlochower, R. Gomez, S. Husa, L. Lehner, and J. Winicour, Mode coupling in the nonlinear response of black holes, Phys. Rev. D **68**, 084014 (2003).

[128] K. Ioka and H. Nakano, Second and higher-order quasinormal modes in binary black hole mergers, Phys. Rev. D **76**, 061503 (2007).

[129] H. Nakano and K. Ioka, Second order quasi-normal mode of the Schwarzschild black hole, Phys. Rev. D **76**, 084007 (2007).

[130] S. Okuzumi, K. Ioka, and M.-a. Sakagami, Possible discovery of nonlinear tail and quasinormal modes in black hole ringdown, Phys. Rev. D **77**, 124018 (2008).

[131] E. Pazos, D. Brizuela, J. M. Martin-Garcia, and M. Tiglio, Mode coupling of Schwarzschild perturbations: Ringdown frequencies, Phys. Rev. D **82**, 104028 (2010).

[132] L. Sberna, P. Bosch, W. E. East, S. R. Green, and L. Lehner, Nonlinear effects in the black hole ringdown: Absorption-induced mode excitation, Phys. Rev. D **105**, 064046 (2022).

[133] E. W. Leaver, Spectral decomposition of the perturbation response of the schwarzschild geometry, Phys. Rev. D **34**, 384 (1986).

[134] N. Oshita, Ease of excitation of black hole ringing: Quantifying the importance of overtones by the excitation factors, Phys. Rev. D **104**, 124032 (2021).

[135] C. T. Cunningham, R. H. Price, and V. Moncrief, Radiation from collapsing relativistic stars. I. Linearized odd-parity radiation, Astrophys. J. **224**, 643 (1978).

[136] C. T. Cunningham, R. H. Price, and V. Moncrief, Radiation from collapsing relativistic stars. II. Linearized even-parity radiation, Astrophys. J. **230**, 870 (1979).

[137] D. A. Nichols and Y. Chen, A hybrid method for understanding black-hole mergers: Head-on case, Phys. Rev. D **82**, 104020 (2010).

[138] D. A. Nichols and Y. Chen, Hybrid method for understanding black-hole mergers: Inspiralling case, Phys. Rev. D **85**, 044035 (2012).

[139] É. É. Flanagan and S. A. Hughes, Measuring gravitational waves from binary black hole coalescences. I. Signal to noise for inspiral, merger, and ringdown, Phys. Rev. D **57**, 4535 (1998).

[140] E. Berti, V. Cardoso, and M. Casals, Eigenvalues and eigenfunctions of spin-weighted spheroidal harmonics in four and higher dimensions, Phys. Rev. D **73**, 024013 (2006); **73**, 109902(E) (2006).

[141] E. Berti and A. Klein, Mixing of spherical and spheroidal modes in perturbed Kerr black holes, Phys. Rev. D **90**, 064012 (2014).

[142] L. London and E. Fauchon-Jones, On modeling for Kerr black holes: Basis learning, QNM frequencies, and spherical-spheroidal mixing coefficients, Classical Quantum Gravity **36**, 235015 (2019).

[143] A. Dhani and B. S. Sathyaprakash, Overtones, mirror modes, and mode-mixing in binary black hole mergers, arXiv:2107.14195.

[144] L. C. Stein, qnm: A Python package for calculating Kerr quasinormal modes, separation constants, and spherical-spheroidal mixing coefficients, J. Open Source Software **4**, 1683 (2019).

[145] F. J. Zerilli, The gravitational field of a particle falling in a Schwarzschild geometry analyzed in tensor harmonics, Ph.D. thesis, Princeton University, 1969.

[146] S. A. Teukolsky, Rotating Black Holes: Separable Wave Equations for Gravitational and Electromagnetic Perturbations, Phys. Rev. Lett. **29,** 1114 (1972).

[147] S. A. Teukolsky, Perturbations of a rotating black hole. I. Fundamental equations for gravitational, electromagnetic, and neutrino-field perturbations, Astrophys. J. **185,** 635 (1973).

[148] S. A. Teukolsky and W. H. Press, Perturbations of a rotating black hole. III—Interaction of the hole with gravitational and electromagnetic radiation, Astrophys. J. **193,** 443 (1974).

[149] S. Mano, H. Suzuki, and E. Takasugi, Analytic solutions of the Teukolsky equation and their low frequency expansions, Prog. Theor. Phys. **95,** 1079 (1996).

[150] S. Ma, Q. Wang, N. Deppe, F. Hébert, L. E. Kidder, J. Moxon, W. Throwe, N. L. Vu, M. A. Scheel, and Y. Chen, Gravitational-wave echoes from numerical-relativity waveforms via spacetime construction near merging compact objects, Phys. Rev. D **105,** 104007 (2022).

[151] M. Boyle *et al.*, The SXS Collaboration catalog of binary black hole simulations, Classical Quantum Gravity **36,** 195006 (2019).

[152] B. J. Kelly and J. G. Baker, Decoding mode mixing in black-hole merger ringdown, Phys. Rev. D **87,** 084004 (2013).

[153] M. Boyle, Transformations of asymptotic gravitational-wave data, Phys. Rev. D **93,** 084031 (2016).

[154] S. Ma *et al.* (to be published).

[155] K. Mitman *et al.*, Fixing the BMS frame of numerical relativity waveforms with BMS charges, arXiv:2208.04356.

[156] K. Mitman *et al.*, Fixing the BMS frame of numerical relativity waveforms, Phys. Rev. D **104,** 024051 (2021).

[157] Black Hole Perturbation Toolkit (bhptoolkit.org).

[158] K. Mitman *et al.*, Nonlinearities in black hole ringdowns, arXiv:2208.07380.

[159] M. H.-Y. Cheung *et al.*, Nonlinear effects in black hole ringdown, arXiv:2208.07374.

[160] L. E. Kidder *et al.*, SpECTRE: A task-based discontinuous Galerkin code for relativistic astrophysics, J. Comput. Phys. **335,** 84 (2017).

[161] N. Deppe *et al.*, SpECTRE v2022.06.14, 10.5281/zenodo.6643787 (2022).

[162] H.-P. Nollert, About the significance of quasinormal modes of black holes, Phys. Rev. D **53,** 4397 (1996).

[163] E. Barausse, V. Cardoso, and P. Pani, Environmental effects for gravitational-wave astrophysics, J. Phys. Confr. Ser. **610,** 012044 (2015).

[164] E. Barausse, V. Cardoso, and P. Pani, Can environmental effects spoil precision gravitational-wave astrophysics?, Phys. Rev. D **89,** 104059 (2014).

[165] J. L. Jaramillo, R. Panosso Macedo, and L. Al Sheikh, Pseudospectrum and Black Hole Quasinormal Mode Instability, Phys. Rev. X **11,** 031003 (2021).

[166] M. H.-Y. Cheung, K. Destounis, R. P. Macedo, E. Berti, and V. Cardoso, Destabilizing the Fundamental Mode of

Black Holes: The Elephant and the Flea, Phys. Rev. Lett. **128,** 111103 (2022).

[167] E. Berti, V. Cardoso, M. H.-Y. Cheung, F. Di Filippo, F. Duque, P. Martens, and S. Mukohyama, Stability of the fundamental quasinormal mode in time-domain observations against small perturbations, Phys. Rev. D **106,** 084011 (2022).

[168] K. Kyutoku, H. Motohashi, and T. Tanaka, Quasinormal modes of Schwarzschild black holes on the real axis, arXiv:2206.00671.

[169] L. Hui, D. Kabat, and S. S. C. Wong, Quasinormal modes, echoes and the causal structure of the Green's function, J. Cosmol. Astropart. Phys. 12 (2019) 020.

[170] V. Cardoso, S. Hopper, C. F. B. Macedo, C. Palenzuela, and P. Pani, Gravitational-wave signatures of exotic compact objects and of quantum corrections at the horizon scale, Phys. Rev. D **94,** 084031 (2016).

[171] H. R. Beyer, On the completeness of the quasinormal modes of the Poschl-Teller potential, Commun. Math. Phys. **204,** 397 (1999).

[172] N. Szpak, Quasinormal mode expansion and the exact solution of the Cauchy problem for wave equations, arXiv:gr-qc/0411050.

[173] H.-P. Nollert and R. H. Price, Quantifying excitations of quasinormal mode systems, J. Math. Phys. (N.Y.) **40,** 980 (1999).

[174] E. S. C. Ching, P. T. Leung, W. M. Suen, and K. Young, Quasinormal Mode Expansion for Linearized Waves in Gravitational System, Phys. Rev. Lett. **74,** 4588 (1995).

[175] S. T. McWilliams, Analytical Black-Hole Binary Merger Waveforms, Phys. Rev. Lett. **122,** 191102 (2019).

[176] S. Ma, M. Giesler, V. Varma, M. A. Scheel, and Y. Chen, Universal features of gravitational waves emitted by superkick binary black hole systems, Phys. Rev. D **104,** 084003 (2021).

[177] B. Chen, Q. Wang, and Y. Chen, Tidal response and near-horizon boundary conditions for spinning exotic compact objects, Phys. Rev. D **103,** 104054 (2021).

[178] A. A. Starobinsky, Amplification of waves reflected from a rotating "black hole", Sov. Phys. JETP **37,** 28 (1973).

[179] D. J. A. McKechan, C. Robinson, and B. S. Sathyaprakash, A tapering window for time-domain templates and simulated signals in the detection of gravitational waves from coalescing compact binaries, Classical Quantum Gravity **27,** 084020 (2010).

[180] F. Zhang, A. Zimmerman, D. A. Nichols, Y. Chen, G. Lovelace, K. D. Matthews, R. Owen, and K. S. Thorne, Visualizing spacetime curvature via frame-drag vortexes and tidal tendexes II. Stationary black holes, Phys. Rev. D **86,** 084049 (2012).

[181] S. Xin, B. Chen, R. K. L. Lo, L. Sun, W.-B. Han, X. Zhong, M. Srivastava, S. Ma, Q. Wang, and Y. Chen, Gravitational-wave echoes from spinning exotic compact objects: Numerical waveforms from the Teukolsky equation, Phys. Rev. D **104,** 104005 (2021).

[182] M. Boyle, L. E. Kidder, S. Ossokine, and H. P. Pfeiffer, Gravitational-wave modes from precessing black-hole binaries, arXiv:1409.4431.